

Photometric Selection of type 1 Quasars in the XMM-LSS Field with Machine Learning and the Disk-Corona Connection

JIAN HUANG,^{1,2} BIN LUO,^{1,2} W. N. BRANDT,^{3,4,5} YING CHEN,^{1,2} QINGLING NI,⁶ YONGQUAN XUE,^{7,8} AND ZIJIAN ZHANG^{9,1}

¹*School of Astronomy and Space Science, Nanjing University, Nanjing, Jiangsu 210093, People's Republic of China*

²*Key Laboratory of Modern Astronomy and Astrophysics (Nanjing University), Ministry of Education, Nanjing 210093, People's Republic of China*

³*Department of Astronomy & Astrophysics, 525 Davey Lab, The Pennsylvania State University, University Park, PA 16802, USA*

⁴*Institute for Gravitation and the Cosmos, The Pennsylvania State University, University Park, PA 16802, USA*

⁵*Department of Physics, 104 Davey Lab, The Pennsylvania State University, University Park, PA 16802, USA*

⁶*Max-Planck-Institut für extraterrestrische Physik (MPE), Gießenbachstraße 1, D-85748 Garching bei München, Germany*

⁷*CAS Key Laboratory for Research in Galaxies and Cosmology, Department of Astronomy, University of Science and Technology of China, Hefei 230026, China*

⁸*School of Astronomy and Space Sciences, University of Science and Technology of China, Hefei 230026, China*

⁹*Department of Astronomy, School of Physics, Peking University, Beijing 100871, People's Republic of China*

ABSTRACT

We present photometric selection of type 1 quasars in the $\approx 5.3 \text{ deg}^2$ XMM-Large Scale Structure (XMM-LSS) survey field with machine learning. We constructed our training and blind-test samples using spectroscopically identified SDSS quasars, galaxies, and stars. We utilized the XGBoost machine learning method to select a total of 1591 quasars. We assessed the classification performance based on the blind-test sample, and the outcome was favorable, demonstrating high reliability ($\approx 99.9\%$) and good completeness ($\approx 87.5\%$). We used XGBoost to estimate photometric redshifts of our selected quasars. The estimated photometric redshifts span a range from 0.41 to 3.75. The outlier fraction of these photometric redshift estimates is $\approx 17\%$ and the normalized median absolute deviation (σ_{NMAD}) is ≈ 0.07 . To study the quasar disk-corona connection, we constructed a subsample of 1016 quasars with HSC $i < 22.5$ after excluding radio-loud and potentially X-ray-absorbed quasars. The relation between the optical-to-X-ray power-law slope parameter (α_{OX}) and the 2500 Å monochromatic luminosity ($L_{2500 \text{ \AA}}$) for this subsample is $\alpha_{\text{OX}} = (-0.156 \pm 0.007) \log L_{2500 \text{ \AA}} + (3.175 \pm 0.211)$ with a dispersion of 0.159. We found this correlation in good agreement with the correlations in previous studies. We explored several factors which may bias the $\alpha_{\text{OX}}-L_{2500 \text{ \AA}}$ relation and found that their effects are not significant. We discussed possible evolution of the $\alpha_{\text{OX}}-L_{2500 \text{ \AA}}$ relation with respect to $L_{2500 \text{ \AA}}$ or redshift.

Unified Astronomy Thesaurus concepts: Quasars (1319); Radio quiet quasars (1354); Supermassive black holes (1663); Active galactic nuclei (16); High energy astrophysics (739)

1. INTRODUCTION

Active galactic nuclei (AGNs) are powered by accretion onto supermassive black holes (SMBHs). A large fraction of the AGN radiation is in the optical/UV and X-ray bands, likely originating from the accretion disk and accretion-disk corona, respectively. A significant correlation between the AGN optical/UV emission and X-ray emission has been observed across a broad range of AGN luminosity, typically expressed as a negative correlation between the optical-to-X-ray power-law slope

parameter (α_{OX})¹ and the 2500 Å monochromatic luminosity ($L_{2500 \text{ \AA}}$; e.g., Avni & Tananbaum 1982; Kriss & Canizares 1985; Avni & Tananbaum 1986; Wilkes et al. 1994; Vignali et al. 2003; Strateva et al. 2005; Steffen et al. 2006; Just et al. 2007; Gibson et al. 2008; Green et al. 2009; Grupe et al. 2010; Lusso et al. 2010; Jin et al. 2012; Chiaraluce et al. 2018; Laha et al. 2018; Liu et al. 2021). This correlation can also be described as a non-linear positive correlation between the 2 keV luminosity ($L_{2 \text{ keV}}$) and $L_{2500 \text{ \AA}}$ (e.g., Tananbaum et al.

¹ α_{OX} is defined as $\alpha_{\text{OX}} = -0.3838 \log(f_{2500 \text{ \AA}}/f_{2 \text{ keV}})$, where $f_{2500 \text{ \AA}}$ and $f_{2 \text{ keV}}$ are the flux densities at 2500 Å and 2 keV, respectively.

1979; Avni & Tananbaum 1982, 1986; Wilkes et al. 1994; Strateva et al. 2005; Steffen et al. 2006; Just et al. 2007; Lusso et al. 2010; Lusso & Risaliti 2016; Chiaraluce et al. 2018). These relations indicate an intrinsic disk-corona connection, and they have been used to identify AGNs emitting unusually weak or strong X-ray emission (e.g., Gibson et al. 2008; Miller et al. 2011; Pu et al. 2020; Fu et al. 2022) or to estimate cosmological parameters (e.g., Lusso & Risaliti 2016; Bisogni et al. 2017; Lusso & Risaliti 2017).

The underlying physics for the empirical $\alpha_{\text{OX}}-L_{2500 \text{ \AA}}$ relation remains elusive, and some studies have suggested that it may be driven by more fundamental correlations between α_{OX} and the SMBH mass and/or Eddington ratio (e.g., Steffen et al. 2006; Kubota & Done 2018; Arcodia et al. 2019; Cheng et al. 2020; Liu et al. 2021; Rankine et al. 2024). For example, Liu et al. (2021) proposed that $\alpha_{\text{OX}} = -0.13\log(L_{\text{Bol}}/L_{\text{Edd}}) - 0.10\log M_{\text{BH}} - 0.69$, where $L_{\text{Bol}}/L_{\text{Edd}}$ and M_{BH} are the Eddington ratio and SMBH mass, respectively. In addition, the observed $\alpha_{\text{OX}}-L_{2500 \text{ \AA}}$ relation has significant dispersion ($\approx 0.1-0.2$; e.g., Steffen et al. 2006).² The dispersion might have contributions from several possible effects: a) X-ray obscuration, b) UV extinction, c) intrinsic X-ray weakness, d) host-galaxy contamination in the UV, e) non-simultaneous X-ray and UV measurements. Nevertheless, the majority of the dispersion appears intrinsic (e.g., Vagnetti et al. 2010, 2013). A few studies suggested that the correlation might have a luminosity dependence, as the slope of the relation appears steeper for luminous quasars (e.g., Steffen et al. 2006; Timlin et al. 2020b; Pu et al. 2020). There are also explorations of the X-ray and UV energy dependence (related to the α_{OX} definition) of the relation (e.g., Young et al. 2010; Jin et al. 2012; Signorini et al. 2023; Jin et al. 2024). The α_{OX} parameter has at most a weak anticorrelation with redshift (e.g., Steffen et al. 2006; Just et al. 2007; Green et al. 2009; Lusso et al. 2010; Vagnetti et al. 2010, 2013; Chiaraluce et al. 2018).

It is actually difficult to select a large sample of type 1 AGNs across broad luminosity and redshift ranges to study the $\alpha_{\text{OX}}-L_{2500 \text{ \AA}}$ relation and then explore the underlying disk-corona connection. Optical/UV spectroscopic selection yields large samples of type 1 AGNs, e.g., from the Sloan Digital Sky Survey (SDSS), but they usually lack good X-ray coverage and are limited to luminous quasars. Deep X-ray surveys, such as the Chan-

dra Deep Fields (e.g., Brandt & Hasinger 2005; Brandt & Alexander 2015; Xue 2017), provide a relatively complete AGN sample across the Universe, but the small areas limit the numbers of type 1 AGNs available and it is also very expensive to obtain complete spectroscopic identifications. There are also various systematics and biases to consider when combining samples from different surveys. Therefore, the current studies of the $\alpha_{\text{OX}}-L_{2500 \text{ \AA}}$ relation are either limited by the sample size (a few hundred AGNs) or the luminosity range (luminous quasars only), hampering our ability to address the relevant questions above and understand the AGN disk-corona connection.

A promising approach to construct a large sample of AGNs for studying the disk-corona connection is to utilize medium-depth large-area X-ray surveys. Currently, the XMM-Spitzer Extragalactic Representative Volume Survey (XMM-SERVS) provides a good balance between survey area and X-ray sensitivity (e.g., Chen et al. 2018; Ni et al. 2021). The total area of the three survey fields, XMM-LSS ($\approx 5.3 \text{ deg}^2$), W-CDF-S ($\approx 4.6 \text{ deg}^2$), and ELAIS-S1 ($\approx 3.2 \text{ deg}^2$), is $\approx 13 \text{ deg}^2$. The average X-ray flux limit reaches $9.8 \times 10^{-15} \text{ erg cm}^{-2} \text{ s}^{-1}$ in the 0.5–10 keV band, which is ≈ 0.5 dex lower than that for the generally available X-ray coverage of SDSS quasars (e.g., Lusso & Risaliti 2017; Lyke et al. 2020). For type 1 AGN identification, although there are several spectroscopic surveys available with additional ones ongoing (e.g., see Section 5.1 of Ni et al. 2021), these are far from complete to provide a representative AGN sample. On the other hand, the XMM-SERVS fields are covered by deep multiwavelength imaging surveys from radio to UV (e.g., Table 1 of Chen et al. 2018), and they also belong to the Deep Drilling Fields of the Legacy Survey of Space and Time (LSST) of the Vera C. Rubin Observatory that will have superb photometric monitoring for ≈ 10 years (e.g., Brandt et al. 2018; Scolnic et al. 2018). Thus it is feasible to perform photometric selection of quasars with the multiwavelength photometric data, aided with also morphological information obtained from the imaging data.

Recently, machine-learning techniques have been demonstrated powerful for selecting luminous quasars in large-area surveys. Compared to traditional template-fitting methods, machine-learning approaches are computationally economical, and they are not sensitive to cross-calibration uncertainties among multiple survey data sets (e.g., zero-point offsets; Salvato et al. 2019). Some popular machine-learning methods include traditional statistical techniques (e.g., Richards et al. 2004; Bovy et al. 2011), support vector machines (e.g., Gao et al. 2008; Peng et al. 2012), neural networks (e.g.,

² The dispersion is typically quantified as the standard deviation of the $\Delta\alpha_{\text{OX}}$ values in different luminosities bins, where $\Delta\alpha_{\text{OX}}$ is the difference between the observed α_{OX} and the expected one from the $\alpha_{\text{OX}}-L_{2500 \text{ \AA}}$ relation: $\Delta\alpha_{\text{OX}} = \alpha_{\text{OX}} - \alpha_{\text{OX, exp}}$.

Yèche et al. 2010; Tuccillo et al. 2015; Chaini et al. 2023; Martínez-Solaeché et al. 2023), Skew-QSO method (Yang et al. 2017; Yang & Shen 2023), and XGBoost (Extreme Gradient Boosting; Chen & Guestrin 2016). Among these techniques, XGBoost has been widely used in classifications among quasars, galaxies, and stars (e.g., Mirabal et al. 2016; Jin et al. 2019; Fu et al. 2021; Golob et al. 2021; Hughes et al. 2022; Calderone et al. 2024; Fu et al. 2024). The advantages of XGBoost include parallel processing, regularization that reduces model overfitting, and a built-in routine to handle missing values. Typically, machine-learning identification of AGNs has been applied to select luminous quasars (e.g., $i < 21.5$; e.g., Jin et al. 2019; Fu et al. 2021). However, the method should also be applicable to lower luminosity quasars as the AGN infrared (IR)–UV spectral energy distributions (SEDs) do not have a strong dependence on luminosity (e.g., Richards et al. 2006; Krawczyk et al. 2013). Besides quasar selection, the machine-learning technique has also been applied to derive quasar photometric redshifts. Compared to the traditional SED fitting approach, machine-learning algorithms are able to infer photometric redshifts with comparable quality (e.g., Sánchez et al. 2014; Beck et al. 2017; Tanaka et al. 2018; Schmidt et al. 2020). Owing to the featureless power-law shape of the quasar optical SED, it is important to include UV, near-IR (NIR), and IR data in the process.

In this study, we use the XGBoost algorithm to photometrically select quasars in the $\approx 5.3 \text{ deg}^2$ XMM-LSS field. We chose relatively conservative criteria to construct a reliable quasar sample, and then we derived photometric redshifts for objects without spectroscopic redshifts. Finally, we selected a subsample of these quasars to study the $\alpha_{\text{OX}}-L_{2500 \text{ \AA}}$ relation with the XMM-SERVS X-ray data. This approach can be applied to the other two XMM-SERVS fields to assemble a larger sample, which we defer to future work. The paper is organized as follows. In Section 2, we describe the multiwavelength data and the construction of the parent, training, and blind-test samples. In Section 3, we present our machine-learning processes and the quasar selection results. Photometric redshifts for our selected quasars are derived in Section 4. In Section 5, we study the $\alpha_{\text{OX}}-L_{2500 \text{ \AA}}$ relation for a subsample of 1007 quasars. We summarize our results in Section 6. Throughout this paper, we adopt a cosmology of $H_0 = 67.4 \text{ km s}^{-1} \text{ Mpc}^{-1}$, $\Omega_{\text{M}} = 0.315$, and $\Omega_{\Lambda} = 0.685$ (Planck Collaboration et al. 2020). The 2500 Å monochromatic luminosity ($L_{2500 \text{ \AA}}$) is expressed in units of $\text{erg s}^{-1} \text{ Hz}^{-1}$.

2. MULTIWAVELENGTH PHOTOMETRY AND SAMPLE CONSTRUCTION

2.1. Multiwavelength Photometric Catalogs

The XMM-LSS field has superb multiwavelength photometric coverage spanning from radio to UV. For our study, we primarily utilized the catalogs in the IR, NIR, optical, and UV bands. All the magnitude measurements have been PSF-corrected.

The IR catalog utilized in this study is the Spitzer DeepDrill XMM-LSS two-band catalog (Lacy et al. 2020, 2021).³ The Spitzer DeepDrill survey covers the entire XMM-LSS field, using the Spitzer Infrared Array Camera (IRAC) 3.6 μm and 4.5 μm filters. This survey achieves a 5σ point-source depth of 2 μJy (corresponding to an AB magnitude of 23.1) in each of the two bands. The full width at half maximum (FWHM) of the point spread function (PSF) for the IRAC 3.6 μm band is approximately $2''$. We adopted the Spitzer DeepDrill $1.9''$ -radius aperture photometry at IRAC 3.6 μm and 4.5 μm bands in this study.

The NIR catalog is the VISTA Deep Extragalactic Observations survey (VIDEO; Jarvis et al. 2013) Data Release 5 (DR5) catalog. Within the XMM-Newton field, the VIDEO survey covers an area of $\approx 4.5 \text{ deg}^2$ in the Z , Y , J , H , and K_{S} bands. This survey reaches a 5σ AB-magnitude depth of $K_{\text{S}} = 23.8$ with a $2''$ -diameter aperture. We adopted the VIDEO $2''$ -diameter aperture photometry in the J , H , and K_{S} bands in this study, and we only selected those objects with SEXTRACTOR flags ≤ 3 (Bertin & Arnouts 1996).

The optical catalog is the Hyper Suprime-Cam Subaru Strategic Programme Data Release 3 catalog (HSC-SSP DR3; Aihara et al. 2022).⁴ This catalog contains imaging data collected with five broad-band filters (g , r , i , z , and y). Within the XMM-LSS field, HSC-SSP has three layers of surveys, including the Wide (covers the entire XMM-LSS field), Deep ($\approx 5 \text{ deg}^2$), and UltraDeep ($\approx 1.77 \text{ deg}^2$) surveys (Aihara et al. 2018). The 5σ limiting magnitudes in the i band for the HSC Wide survey and combined Deep/UltraDeep survey (processed jointly since DR2) are 26.2 and 26.9, respectively (Aihara et al. 2022). The median FWHM of the HSC-SSP i -band PSF is $0''.69$ (Miyazaki et al. 2018). In this study, we adopted the PSF magnitudes in the five bands to construct colors, and we used the differences between the PSF and Kron magnitudes (e.g., $i_{\text{PSF}} - i_{\text{Kron}}$) in the five bands as indicators of source morphology (e.g., Jin et al. 2019; Fu et al. 2021).

³ <https://irsa.ipac.caltech.edu/cgi-bin/Gator/nph-dd>.

⁴ https://hsc-release.mtk.nao.ac.jp/doc/index.php/faq_pdr3.

The UV catalogs are the Canada-France-Hawaii Telescope Legacy Survey (CFHTLS; Hudelot et al. 2012) and GALEX Deep Imaging Survey (Martin et al. 2005) catalogs. CFHTLS comprises two survey layers in the XMM-LSS field: a wide layer (CFHTLS-W1) covering the entire 5.3 deg^2 XMM-LSS field, and a deep layer (CFHTLS-D1) covering a 1 deg^2 region. The CFHTLS-W1 catalog reaches an 80% completeness limit of $u^* = 25.2$ for point sources, and the CFHTLS-D1 catalog has an 80% completeness limit of $u^* = 26.3$. The average PSF FWHM for the CFHTLS u^* band is $\approx 0''.85$. The GALEX Deep Imaging Survey covers the entire XMM-LSS field. Within this area, the 99% limiting magnitude in the near-UV (NUV) band is ≈ 25.3 . The 80% PSF sizes in the GALEX NUV and far-UV (FUV) bands are both $\approx 6''$. We adopted the $3''$ -diameter aperture photometry in the u^* band from the CFHTLS catalogs and the calibrated fluxes in the FUV and NUV bands from the GALEX catalog. We excluded CFHTLS and GALEX sources with SEXTRACTOR flags > 3 . We also excluded those GALEX sources labeled with artifacts = 2 or 4 following the GALEX official instructions.⁵

2.2. Parent Sample Construction

We selected our parent-sample sources from the HSC DR3 catalog. We adopted additional filtering criteria based on data quality, IR detections, and source blending.

1. We selected HSC sources from a circular region with a radius of $1^\circ.9$ (an area of $\approx 11 \text{ deg}^2$) centering at RA = $35^\circ.5743$ and DEC = $-4^\circ.7485$. As shown in Figure 1, this region completely covers the XMM-SERVS XMM-LSS field. This circular region is an approximation of the Spitzer DeepDrill survey field so that we have good Spitzer IRAC photometric coverage.
2. We set an i -band magnitude cut of $i < 23$. Given the 50% full-band flux limit of $4.4 \times 10^{-15} \text{ erg cm}^{-2} \text{ s}^{-1}$ in the XMM-SERVS XMM-LSS survey (Chen et al. 2018), we estimate that quasars with $i < 22.5$ and redshift up to ≈ 2.3 (corresponding to $\approx 85\%$ of the training-sample quasars) can be detected, if they exhibit nominal levels of X-ray emission as expected from the $\alpha_{\text{OX}}-L_{2500 \text{ \AA}}$ relation of Just et al. (2007). We relaxed the criterion to $i < 23$ in the quasar selection stage.
3. Referring to the HSC official instructions, we selected HSC Wide-layer and Deep/UltraDeep-layer catalog sources with clean photometry by excluding those with bad pixels, cosmic rays in the source centers, pixels outside the usable exposure regions, or bad centroids. We required each HSC source to have all the 5-band photometric measurements in order to obtain its comprehensive colors. To obtain reliable morphological features in each band (e.g., $i_{\text{PSF}} - i_{\text{Kron}}$) which is useful for distinguishing point sources (quasars and stars) from extended sources (galaxies), we also excluded sources with flags of problematic PSF-magnitude or Kron-magnitude measurements. We merged the HSC Wide-layer and Deep/UltraDeep-layer catalogs using a $1''$ -matching radius, with the Deep/UltraDeep-layer catalog having a higher priority. We then obtained a sample of 259 707 HSC sources with HSC $i < 23$.
4. We required that every source must have Spitzer DeepDrill IRAC measurements, as mid-infrared-related colors are critical for quasar selection and photometric redshift estimation (e.g., Jin et al. 2019; Fu et al. 2021). All type 1 quasars with $i < 23$ are expected to be detectable in the Spitzer DeepDrill survey considering the typical quasar SED in Krawczyk et al. (2013). We excluded Spitzer DeepDrill sources with flux densities smaller than their uncertainties or SEXTRACTOR flags > 3 in either of the two IRAC bands. We then matched the Spitzer DeepDrill sources to the HSC sources using a $1''$ -matching radius and obtained 184 140 matches. There are 142 pairs where two HSC sources matched to one IRAC source. For the rest 183 856 (184 140–284) matches, all HSC sources has a one-to-one match to a unique Spitzer DeepDrill source.
5. The HSC-SSP survey has a better spatial resolution than the Spitzer DeepDrill survey (Section 2.1), and thus one Spitzer DeepDrill IRAC source might be the blend of two neighbouring HSC sources. We considered an HSC source as potentially IRAC blended if there are other $i < 25.5$ HSC sources within $2''$ and these $i < 25.5$ HSC sources have no other matched IRAC sources, and subsequently excluded it. All of the 142 pairs with two HSC sources matched to one IRAC source are excluded in this filtering process. This filtering process resulted in a sample of 168 905 HSC sources, and all of them have a one-to-one match to an unique IRAC source.

⁵ <https://galex.stsci.edu/GR6/?page=ddfaq#6>.

When matching the 168 905 HSC sources to the VIDEO sources using a $1''$ -matching radius, we found that there are 100 HSC sources with multiple VIDEO counterparts. We checked the HSC images of these sources and found that they are likely blended with nearby sources, which were not identified in the HSC source catalogs. We then excluded these sources and obtained 168 805 sources. These objects constitute our parent sample.

We show the spatial distribution of the parent-sample sources in Figure 1. In Table 1, we list the fraction of our parent-sample sources with available HSC and Spitzer IRAC photometry. For a small number ($\approx 0.1\%$) of parent-sample sources, they do not have Kron photometry in one or more specific HSC bands and are still labeled as sources with Kron photometry in the HSC DR3 source catalog. As a result, the fraction of parent-sample sources with available Kron photometry in a specific HSC band is not 100%. The Kron-magnitude-related colors of sources without Kron photometry are treated as missing values in our selection stage (see Section 3 below). The distribution of the i -band magnitudes of the parent-sample sources is shown in Figure 2. The parent-sample sources have an average i -band magnitude of 21.7. All parent-sample sources are detected in the HSC g , r , i , z , and y bands (with available PSF photometry) and Spitzer DeepDrill IRAC $3.6 \mu\text{m}$ and $4.5 \mu\text{m}$ bands, as per the sample construction.

2.3. VIDEO NIR, CFHTLS u -band and GALEX UV Photometry

For each of the sources in our parent sample, the VIDEO J -, H -, K_S -band photometric measurements were collected by matching the VIDEO catalog sources to its HSC coordinate using a $1''$ -matching radius. In Table 1, we list the fraction of our parent-sample sources with available VIDEO photometry; only $\approx 50\%$ of our parent-sample sources have available VIDEO photometry due to the limited coverage of the VIDEO survey field (see Figure 1). All parent sample objects within the VIDEO footprint have VIDEO counterparts, except for a few sources that are located near bright stars or galaxies, which might have affected the VIDEO photometric extraction.

We searched for the u^* -band measurements from the CFHTLS source catalogs for the parent sample. We matched the HSC parent-sample sources to the CFHTLS-D1 and CFHTLS-W1 sources using an $1''$ -matching radius to obtain the u^* -band measurements, and the CFHTLS-D1 photometry is preferred.

Table 1. Summary of Sample Photometry

Survey	Parent	Training	Blind-test
Band	Sample	Sample	Sample
(1)	(2)	(3)	(4)
GALEX FUV	17.2%	18.3%	18.5%
GALEX NUV	30.7%	49.6%	44.2%
CFHTLS u^*	86.0%	99.3%	67.9%
HSC g , r , i , z , and y (PSF)	100.0%	100.0%	100.0%
VIDEO J	50.8%	80.9%	16.8%
VIDEO H	50.8%	80.9%	16.8%
VIDEO K_S	50.8%	81.0%	16.8%
DeepDrill IRAC [3.6] and [4.5]	100.0%	100.0%	100.0%
HSC g_{Kron}	99.9%	99.9%	99.9%
HSC r_{Kron}	99.9%	99.9%	99.9%
HSC i_{Kron}	99.9%	99.9%	99.9%
HSC z_{Kron}	99.9%	99.9%	99.9%
HSC y_{Kron}	99.8%	99.9%	99.8%

NOTE—Column (1): name of the survey band. Columns (2)-(4): fraction of the parent sample, training sample, and blind-test sample sources with available photometry in each band, respectively. A small number ($\approx 0.1\%$) of parent-sample sources do not have Kron photometry in one or more specific HSC bands and are still labeled as sources with Kron photometry in the HSC DR3 source catalog. Therefore, the fraction of parent-sample sources with available Kron photometry in a specific HSC band is not 100%.

In Table 1, we list the fraction of our parent-sample sources with available CFHTLS u^* -band photometry.

We collected the UV measurements from the GALEX Deep Imaging Survey source catalog for our parent sample. A source in the XMM-LSS field usually has multiple GALEX measurements in the GALEX source catalog. Following a method similar to that adopted by Zou et al. (2022), we selected unique measurements for each GALEX source. We first ranked all GALEX catalog sources according to their detection status: sources with detection in both NUV and FUV bands were ranked at the top, while sources with only NUV or FUV detection were ranked in the middle and the bottom. Then, for sources within each level of detection status, we assigned higher rankings to those with longer exposure times. Among sources with the same detection status and exposure times, we assigned higher rankings to those with smaller `fov_radius` values. To construct our unique source catalog, we matched each GALEX source with a high rank to the GALEX sources with lower ranks with a matching radius of $2.5''$, and we excluded the matched sources with lower ranks. Then we matched the unique

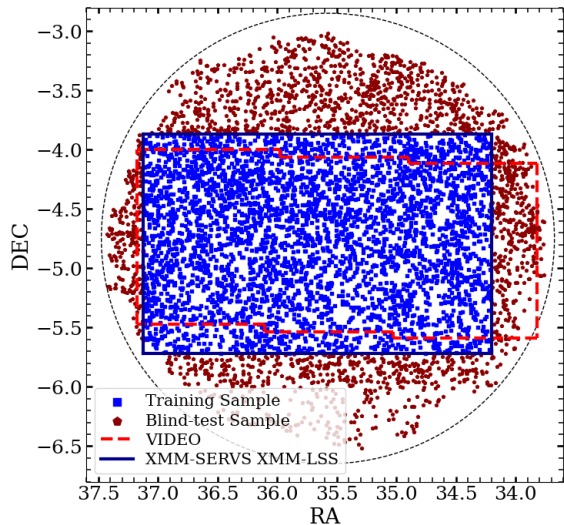


Figure 1. Spatial distributions of our sample sources. The circle represents the region we used to select initial HSC catalog sources which is an approximation of the Spitzer Deep-Drill field. The red dashed line represents the VIDEO survey field. The dark-blue solid line represents the X-ray source catalog selection area in Chen et al. (2018). The blue squares and the dark-red pentagons represent the training-sample sources and blind-test-sample sources, respectively. Individual parent sample sources are not shown, but except small cavities which may be caused by bright stars and bad pixels, the spatial distribution of our parent-sample sources is pretty uniform.

GALEX sources to our parent-sample sources using an $1''$ -matching radius. In Table 1, we list the fraction of our parent-sample sources with available GALEX photometry.

2.4. Spectroscopic Training Sample

From the parent sample, we selected spectroscopically confirmed quasars from the SDSS Data Release 16 quasar catalog (Lyke et al. 2020) in the XMM-LSS field as the training-sample quasars. We matched these SDSS DR16 quasars to the HSC coordinates of our parent-sample sources using a $1''$ -matching radius and obtained 1260 matched quasars. To ensure that the spectroscopically confirmed quasars are indeed type 1 quasars with reliable redshift measurements, we selected 1116 SDSS quasars with no pipeline warning on its redshift measurement ($z_{\text{warning}} = 0$).

From sources in the SpecPhotoAll table of SDSS DR16, we utilized CASJOB to extract a sample of spectroscopically identified galaxies and stars with $z_{\text{warning}} = 0$. Subsequently, we matched these galaxies and stars to our parent-sample sources using a $1''$ -matching radius. We then selected those parent-sample sources with matched SDSS spectra in-

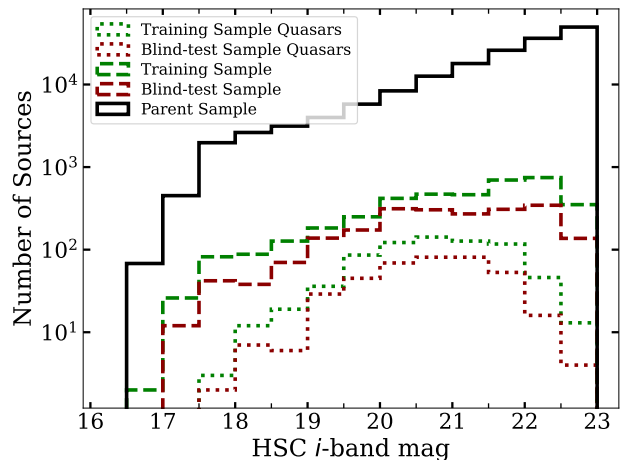


Figure 2. Distribution of the observed i -band magnitude of our parent-sample, training-sample, and blind-test-sample sources. The training and blind-test-sample sources are brighter than the parent-sample sources, which is attributed to the target selection strategies utilized in SDSS spectroscopic observations.

side the XMM-SERVS XMM-LSS field as our training sample. Our training sample comprises 723 quasars, 2673 galaxies, and 314 stars. We list these numbers in Table 2. The spatial distribution of the training sample objects is illustrated in Figure 1.

We display the distribution of the observed i -band magnitudes for the training-sample sources in Figure 2. With an average i -band magnitude of 20.7, the training sample quasars are brighter than the parent sample with an average i -band magnitude of 21.7. This is because optically bright sources are preferred in SDSS spectroscopic observations. Details regarding the fraction of our training-sample sources with available photometry are listed in Table 1. Compared to the entire parent sample, our training-sample sources exhibit a significantly higher fraction of available photometry in the VIDEO J , H , and K_S bands, primarily due to the coverage of the VIDEO survey field, which is in the XMM-LSS field (Figure 1).

2.5. Blind-Test Sample

In machine learning, models often capture patterns specific to the training sample, leading to high accuracy on the training sample but poor performance on new, unseen data. A blind-test sample, that is not included in the training procedure, is thus typically needed; it enables the evaluation of how well the model generalizes to unseen data. The blind-test sample is essential for identifying issues such as overfitting, where a model performs well on the training data but poorly on new data. Therefore, we created a blind-test sample from the

parent-sample sources located outside the XMM-SERVS XMM-LSS field.

The blind-test sample was constructed from the SDSS DR16 catalogs in the same manner as the training sample (Section 2.4), resulting in 393 quasars, 1503 galaxies, and 155 stars. We list these numbers in Table 2. The spatial distribution of the blind-test sample objects is displayed in Figure 1. We present the distribution of the observed i -band magnitudes for the blind-test sample sources in Figure 2. The distribution of observed i -band magnitudes for our blind-test-sample quasars aligns with that of our training-sample quasars, both having an average i -band magnitude of 20.7. We present the fraction of available photometry in each band for our blind-test-sample sources in Table 1. When compared to our training-sample sources, the blind-test-sample sources show significantly lower fractions of available CFHTLS u^* and VIDEO J , H , K_S photometry. All blind-test-sample sources are located outside the XMM-LSS field, and only a few of them have VIDEO coverage. Furthermore, blind-test-sample sources with declinations larger than $-3^\circ.705$ also lack CFHTLS coverage.

3. PHOTOMETRIC SELECTION OF QUASARS

In this study, we utilized XGBoost to construct our quasar selection procedure. We developed two classifiers: the first to differentiate extragalactic objects (quasars and galaxies) from stars, and the second to specifically identify quasars while excluding galaxies. In the first classifier, quasars and galaxies are grouped together based on the rationale that quasars are essentially a unique subclass of galaxies. In principle, a single three-class classifier is capable of performing similar selections. However, the two-classifier approach could reduce the impact of class imbalance (see discussion in Section 3.3 of Fu et al. 2021), making it easier to fine-tune the hyperparameters for underrepresented classes (i.e., quasars in the case here). It also allows each binary classifier to use tailored features or thresholds that might not apply universally in a three-class classifier, which may improve model accuracy for each step. The sample used to train the first classifier includes 314 stars and 3396 extragalactic objects; for the second classifier, the training sample consists of the 3396 extragalactic objects with 723 quasars and 2673 galaxies (see Section 2.4).

3.1. Input Features

Our sample sources were characterized by input features consisting of 18 colors ($FUV - NUV$, $NUV - u^*$, $NUV - g$, $u^* - g$, $g - r$, $r - i$, $i - z$, $z - y$, $y - J$,

$J - H$, $H - K_S$, $K_S - IRAC$ [3.6], $IRAC$ [3.6] - [4.5], $g - IRAC$ [3.6], $r - IRAC$ [3.6], $i - IRAC$ [3.6], $z - IRAC$ [3.6], and $y - IRAC$ [3.6]) and 5 morphological parameters ($g_{PSF} - g_{Kron}$, $r_{PSF} - r_{Kron}$, $i_{PSF} - i_{Kron}$, $z_{PSF} - z_{Kron}$, and $y_{PSF} - y_{Kron}$). Besides the first 13 independent colors derived from the photometry of neighboring bands (i.e., $FUV - NUV$ to $IRAC$ [3.6] - [4.5]),⁶ we also included the latter five colors to approximate the optical-to-mid-IR (MIR) SED shape that appeared useful for distinguishing quasars from stars in previous studies (e.g., Jin et al. 2019; Fu et al. 2021). In cases where a source lacks available photometry or has a magnitude error greater than 0.2 in a given band, we denoted the magnitude in that band and its related colors with missing values (represented as “999”). XGBoost incorporates a built-in routine to handle these missing values (see Section 3.4 of Chen & Guestrin 2016). During tree construction, XGBoost assigns a default direction for missing values, allowing it to decide whether to send missing data to the left or right child node based on the optimal gain from that split. This process can be interpreted as XGBoost learning an optimal imputation value for missing data.⁷ To correct for Galactic extinction, we utilized the Milky Way R_V -dependent extinction model by Fitzpatrick et al. (2019) with $R_V = 3.1$, along with Galactic extinction $E(B - V)$ values obtained from the dust map by Schlegel et al. (1998).

3.2. Model Optimization

We utilized OPTUNA (Akiba et al. 2019), an open-source hyperparameter optimization framework, to fine-tune the hyperparameters of XGBoost and obtain the optimal model. The fixed hyperparameters of the XGBoost classifiers are as follows: `colsample_bytree = 1`, `n_estimators = 100`, `objective = binary:logistic`, `seed = 0`, `subsample = 1`, and `tree_method = hist`. These hyperparameters are set to either their default values or values referenced from previous studies (e.g., Jin et al. 2019; Fu et al. 2021). Other hyperparameters were allowed to vary within a grid of values. For example, the hyperparameter `max_depth`,⁸ which defines the maximum depth of a tree, is allowed to vary between 5 and 10. This range promotes simpler models that are less likely to overfit.

We utilized a five-fold cross-validation strategy to find the optimal hyperparameter sets for the two classifiers.

⁶ The color $NUV - g$ is used because not all sources have u^* -band photometry.

⁷ <https://github.com/dmlc/xgboost/issues/21>.

⁸ <https://xgboost.readthedocs.io/en/stable/parameter.html>.

The entire training sample is used for both training and validation. During the five-fold cross validation, the random seed is arbitrarily fixed at 100 for reproducibility. We fine-tuned the model hyperparameters through 5 000 trials to identify the optimal hyperparameter set for each classifier that minimized the average log loss value. The log loss value is defined as:

$$L_{\log}(y, p) = -\frac{1}{N} \sum_{i=1}^N (y \log(p) + (1 - y) \log(1 - p)). \quad (1)$$

Here, N is the number of sample sources, $y \in \{0, 1\}$ represents the true label of a sample, and $p = \Pr(y = 1)$ is the XGBoost-predicted probability estimate of a sample belonging to extragalactic objects or quasars. The log loss value measures the accuracy of the predicted probabilities compared to the actual class labels (0 or 1) for binary classification. The smaller the log loss value is, the better the model performs. For the first and second classifiers, the average log loss values for the optimal hyperparameter sets during the five-fold cross validation are 0.010 and 0.054, respectively.

We also used two metrics, reliability and completeness, to evaluate the performance of the classifiers, which are defined as follows:

$$\text{Reliability} = \frac{\text{TP}}{\text{TP} + \text{FP}}, \quad (2)$$

$$\text{Completeness} = \frac{\text{TP}}{\text{TP} + \text{FN}}, \quad (3)$$

where true positive is denoted as TP, true negative as TN, false positive as FP, and false negative as FN. In the first and second classifiers, TP refers to the correctly predicted extragalactic objects and quasars, respectively. The reliability and completeness values during the five-fold cross validation and the blind-test validation of each classifier are presented in Sections 3.3 and 3.4 below.

3.3. Selection of Extragalactic Objects

To calculate the reliability and completeness for the first classifier, we need to set a threshold on the probability ($p_{\text{extragalactic}}$) provided by XGBoost to determine the numbers of TP, TN, FP, and FN. Therefore, we investigated the relations between the two metrics (reliability and completeness) of predicted extragalactic objects and $p_{\text{extragalactic}}$ from the five-fold cross-validation results, as shown in Figure 3(a). Additionally, we applied the first classifier to the blind-test-sample objects to examine these relations, also shown in Figure 3(a). The representative 1σ statistical uncertainty is shown in the plot,

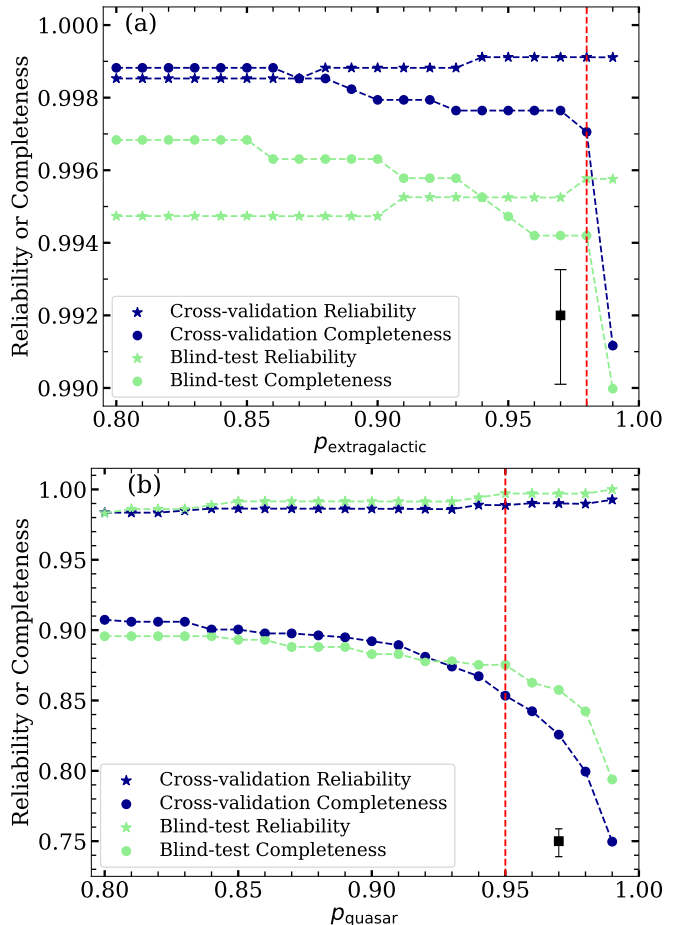


Figure 3. (a) Reliability and completeness of predicted extragalactic objects for the five-fold cross-validation (dark blue points) and blind-test (light green points) results, plotted as a function of $p_{\text{extragalactic}}$. (b) The same as panel (a), but for the predicted quasars from the second classifier. The $p_{\text{extragalactic}}$ and p_{quasar} values range from 0.80 to 0.99, with increments of 0.01. The vertical red dashed lines indicate the thresholds for classifying extragalactic objects ($p_{\text{extragalactic}} > 0.98$) and quasars ($p_{\text{quasar}} > 0.95$). The error bar in the lower right corner in each panel represents the median 1σ statistical uncertainty of the data points. The apparent large difference between the cross-validation and blind-test results in panel (a) is due to the small range of the y -axis values.

derived following Equations 16 and 17 of Gehrels (1986). Since the blind-test-sample objects were not used to train the classifier, their relations provide a suitable means for evaluating the true performance of the classifier on unseen data. The cross-validation and blind-test results agree well (note the small y -axis range in the plot), and as expected, when $p_{\text{extragalactic}}$ increases, the reliability increases but the completeness decreases. Our primary objective in this study is to reliably select a sample of type 1 quasars based on their photometry and

Table 2. Numbers of Sources in Each Sample

Sample	Sources	SDSS Quasars	SDSS Galaxies	SDSS Stars	Quasars Selected by XGBoost
(1)	(2)	(3)	(4)	(5)	(6)
Parent Sample	168805	1116	4176	469	2784 (including 992 SDSS quasars)
Training Sample (in the XMM-LSS field)	3710	723	2673	314	651 (including 651 SDSS quasars)
Blind-test Sample (outside the XMM-LSS field)	2051	393	1503	155	344 (including 343 SDSS quasars)

NOTE— Column (1): the name of samples. Column (2): the number of sample sources. Columns (3)–(5): the number of SDSS quasars, galaxies, and stars. Column (6): the number of sources selected as quasars by XGBoost. Some SDSS quasars are not recovered by XGBoost, and one galaxy in the blind-test sample was misidentified as a quasar by XGBoost.

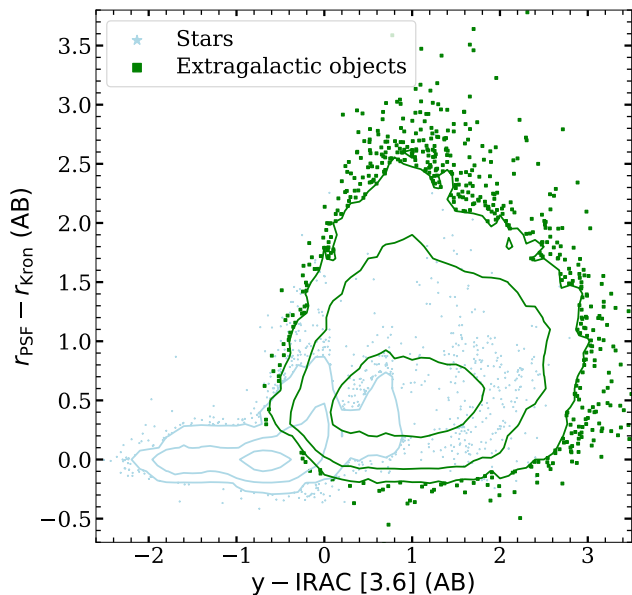


Figure 4. The color-morphology diagram of the stars (light-blue contours) and extragalactic objects (green contours) selected from our parent sample. Contours represent source number densities per bin, with a bin size of 0.1×0.1 along each axis. For extragalactic objects, the contour levels from the outside to the inside are spaced as 5, 50, and 500 per bin, while for stars, the contour levels are spaced as 10, 100, and 1000 per bin.

investigate their disk-corona connection, and thus we need to minimize the biases introduced by stars and galaxies misclassified as quasars. To exclude as many stars as possible and achieve a high completeness of extragalactic objects, we set $p_{\text{extragalactic}} \geq 0.98$ as the threshold to classify extragalactic objects. Beyond this value, the reliability does not improve, but the completeness drops significantly. During the five-fold cross validation, the reliability and completeness of extragalactic objects are 0.9991 and 0.9997, respectively. For stars, the reliability and completeness are 0.9688 and 0.9904,

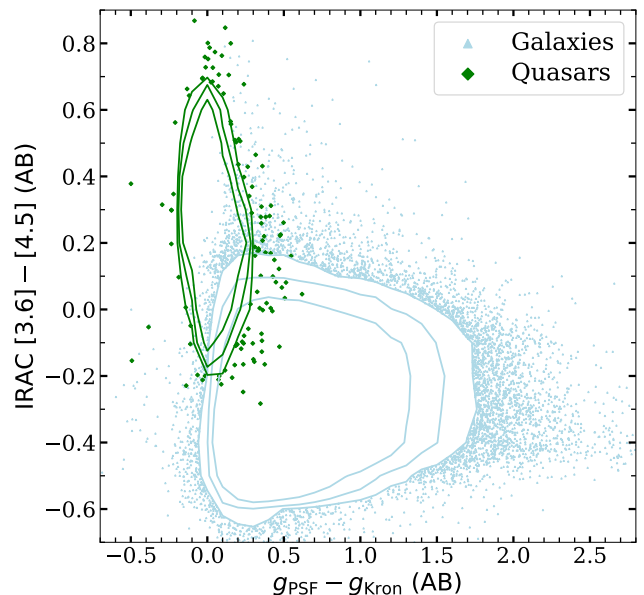


Figure 5. The morphology-color diagram of the galaxies (light-blue contours) and quasars (green contours) selected from our parent sample. Contours represent source number densities per bin, with a bin size of 0.1×0.1 along each axis. For quasars, the contour levels from the outside to the inside are spaced as 8, 16, and 32 per bin, while for galaxies, the contour levels are spaced as 150, 300, and 600 per bin.

respectively. For the blind-test sample, the reliability and completeness of extragalactic objects are 0.9958 and 0.9942, respectively, while for stars, they are 0.9304 and 0.9484, respectively. The blind-test results for stars are also listed in Table 3.

We then applied the first classifier to all parent-sample objects. 135 272 of the parent-sample sources were classified as extragalactic objects, including all of the 723 training-sample quasars. Among the input features, the color $y - \text{IRAC [3.6]}$ and the morphology feature $r_{\text{PSF}} - r_{\text{Kron}}$ carried the highest and second-highest weights, respectively. In Figure 4, we

Table 3. Performance of Our Selection

Classes	Reliability	Completeness
(1)	(2)	(3)
Quasars	$0.997^{+0.002}_{-0.007}$	$0.875^{+0.017}_{-0.019}$
Galaxies	$0.966^{+0.004}_{-0.006}$	$0.995^{+0.002}_{-0.003}$
Stars	$0.930^{+0.021}_{-0.026}$	$0.948^{+0.018}_{-0.024}$

NOTE— The reliability and completeness of the XGBoost selected quasars, galaxies, and stars in the blind-test sample, calculated from the classification results of XGBoost. The errors are 1σ statistical uncertainties calculated following Equations 16 and 17 of (Gehrels 1986).

display our selected extragalactic objects and stars in the $y - \text{IRAC [3.6]}$ versus $r_{\text{PSF}} - r_{\text{Kron}}$ color-morphology feature space. Our selected extragalactic objects generally exhibit redder $y - \text{IRAC [3.6]}$ colors compared to the selected stars. Additionally, the selected extragalactic objects tend to have larger $r_{\text{PSF}} - r_{\text{Kron}}$ values on average, primarily because most of them are galaxies (see Section 3.4 below). These features highlight the importance of MIR photometry and morphology in distinguishing extragalactic objects from stars (e.g., Jin et al. 2019; Fu et al. 2021, 2024).

3.4. Selection of Quasars

For the second classifier, we also investigated the relation between the two metrics (reliability and completeness) of predicted quasars and p_{quasar} , as shown in Figure 3(b). We also applied the second classifier to the quasars and galaxies in the blind-test sample to examine these relations, as shown in Figure 3(b). The two sets of metric values are overall consistent with each other. To create a reliable sample of quasars and strike a balance between reliability and completeness, we adopted $p_{\text{quasar}} \geq 0.95$ as the threshold to classify quasars, referring to the relations of the blind-test sample. During the five-fold cross validation, the reliability and completeness of quasars are 0.9888 and 0.8534, respectively. For galaxies, the reliability and completeness are 0.9618 and 0.9974, respectively. For the blind-test sample, the reliability and completeness of quasars are 0.9971 and 0.8753, respectively, while for galaxies, they are 0.9658 and 0.9947, respectively. The blind-test results for galaxies and quasars are also listed in Table 3.

We then applied the second classifier to the 135 272 extragalactic objects classified by the first classifier, and selected 2 784 quasars. We list the number of quasars selected by XGBoost in Table 2. We selected 1 591 quasars

within the XMM-SERVS XMM-LSS field (Figure 1) from the 2 784 quasars to study their disk-corona connection (see Section 5 below), given their X-ray coverage in this field. These 1 591 quasars include 651 of the SDSS training-sample quasars. The other 72 training-sample quasars were not classified as quasars and they were not included in our study of the disk-corona connection in Section 5 below. These 72 quasars were not correctly classified in this step mainly because we adopted a strict threshold cut (i.e., $p_{\text{quasar}} \geq 0.95$) to ensure high reliability of the selected quasars; many of these 72 quasars have relatively extended morphology, suggestive of higher host-galaxy contamination. Using a lower threshold cut, such as $p_{\text{quasar}} > 0.2$, would include all these 72 quasars. However, this would also increase significantly the numbers of quasars with strong host-galaxy contamination and galaxies misclassified as quasars, potentially biasing the derived $\alpha_{\text{OX}} - L_{2500 \text{ \AA}}$ relation.

In the second classifier model, the morphology feature $g_{\text{PSF}} - g_{\text{Kron}}$ and the color $\text{IRAC [3.6]} - [4.5]$ carried the highest and second-highest weights. In Figure 5, we illustrate the distribution of the selected quasars and galaxies in the $g_{\text{PSF}} - g_{\text{Kron}}$ versus $\text{IRAC [3.6]} - [4.5]$ morphology-color feature space. Compared to our selected galaxies, our chosen quasars are more likely to be point-like sources, and they exhibit redder $\text{IRAC [3.6]} - [4.5]$ colors which are a characteristic feature of typical AGN SEDs. These results highlight the importance of MIR colors and morphology in distinguishing quasars from galaxies in the photometric classification approach (e.g., Fu et al. 2021; Golob et al. 2021; Fu et al. 2024), offering valuable insights for future multi-wavelength surveys.

3.5. Selection Reliability and Completeness

The blind-test-sample objects (see Section 2.5) were not included in the training of the quasar selection model, allowing us to use them to evaluate the performance of our selection. The reliability and completeness values for the three types of objects from the blind-test results are summarized in Table 3. The results are presented in Table 3. The quasar selection is highly reliable; of the 345 selected quasars, 344 are SDSS quasars (Table 2) and only one galaxy was misidentified as a quasar, yielding a reliability of 0.997 (344/345). The quasar selection completeness is 0.875 (344/393), still acceptable. The completeness for the selected quasars is lower than that for the selected galaxies because we utilized a strict threshold for p_{quasar} in this study. Some quasars, particularly those that are outshined by their host galaxies, may be classified as galaxies. Utilizing a lower threshold

would increase the completeness but reduce the reliability, resulting in more galaxies misclassified as quasars that may hamper the study of the $\alpha_{\text{OX}}-L_{2500 \text{ \AA}}$ relation (galaxies are generally not luminous X-ray emitters). Our primary objective in this study is to reliably select a sample of type 1 quasars based on their photometry and investigate their disk-corona connection, making high reliability a top priority. The VIDEO J, H, K_S and CFHTLS u^* coverage for the blind-test sample is less extensive than that for the parent sample in the XMM-LSS field (Table 1), so it is possible that the selection reliability and completeness for the parent-sample sources in the XMM-LSS field might be better.

One of the objectives of our study is to efficiently select a large sample of quasars that extend to lower luminosities compared to previous machine-learning results (see Section 1). Therefore, we examined the evolution of reliability and completeness as a function of the observed i -band magnitude of our blind-test-sample quasars selected by XGBoost, as shown in Figure 6. No significant evolution was observed in the reliability or completeness parameters, probably because the IR-to-UV SED shapes of quasars do not have a strong dependence on luminosity (e.g., Richards et al. 2006; Krawczyk et al. 2013). Compared to previous studies that primarily selected optically brighter quasars for training and identification (e.g., Jin et al. 2019 with $r \lesssim 21.5$ and Fu et al. 2021 with $i \lesssim 22$), our approach is capable of identifying fainter quasars down to $i \approx 22.5$; within the magnitude range of $22 < i < 23$, we selected 649 quasars ($\approx 23\%$ of the 2784 selected quasars).

3.6. Sky Density of Selected Quasars

The sky density of the 2784 XGBoost selected quasars is 253 deg^{-2} ($2784/11 \text{ deg}^{-2}$), which is higher than that of the SDSS DR16 quasars in the same region (101 deg^{-2} ; $1116/11 \text{ deg}^{-2}$). Our quasar sky density is comparable to the sky densities of quasars obtained from spectroscopic identifications of X-ray AGNs in surveys with similar depths; for example, the broad-line AGN density is $\approx 220 \text{ deg}^{-2}$ in the XMM-Newton COSMOS field (e.g., Brusa et al. 2010), and it is $\approx 290 \text{ deg}^{-2}$ in the Chandra COSMOS field (e.g., Marchesi et al. 2016).

For the 1591 selected quasars within the XMM-SERVS XMM-LSS field (Figure 1) that are used to study the disk-corona connection (see Section 5 below), the sky density reaches 300 deg^{-2} ($1591/5.3 \text{ deg}^{-2}$), higher than that (253 deg^{-2}) in the parent sample. The higher density is likely due to the more extensive coverage of the VIDEO and CFHTLS surveys in this field.

3.7. Spectroscopic Validation

Among the 1591 selected quasars in the XMM-SERVS XMM-LSS field, we have obtained spectroscopic observations of 96 quasars using optical telescopes, including the MMT (Hectospec) 6.5-m telescope and the WIYN (Hydra) 3.5-m telescope.

We visually checked the spectra of the 44 quasars with signal-to-noise ratios ≥ 3 in the observed wavelength range of 4000–7000 Å (5000–7000 Å for WIYN/Hydra spectra), a window where telluric-absorption effect is small. We identified 41 objects with clear broad emission lines, categorizing them as reliable quasars. In Figure 7, we provide the spectrum of J022718.28–052613.5 as an example of such quasars. We not only successfully classified this quasar but also obtained an accurate estimate of its redshift ($z_{\text{photo}} = 2.52$ vs. $z_{\text{spec}} = 2.573$; see Section 4 below). We did not find apparent broad emission lines for the other 3 objects, and none of them is X-ray-detected. Among the 3 objects, one is likely a type 2 AGN, with an apparently redder UV/optical continuum compared to the SDSS quasar composite spectrum constructed by Vanden Berk et al. (2001), a clear narrow H β emission line, and a strong set of [O III] doublet. In Figure 8, we show the spectra of the other two objects, J022605.98–052241.7 and J022532.17–050545.6. There are no apparent broad emission lines in the two MMT spectra. For J022605.98–052241.7, the continuum shape is consistent with that of the SDSS quasar composite spectrum, suggesting that it is probably a weak emission-line quasar (WLQ; e.g., Diamond-Stanic et al. 2009; Shemmer et al. 2009; Plotkin et al. 2010; Laor & Davis 2011; Wu et al. 2012). J022532.17–050545.6 has a noisy spectrum, and the continuum is apparently redder than the SDSS quasar composite spectrum. Given its photo- z of 1.04, the only strong broad emission line expected in an AGN spectrum is Mg II $\lambda 2799$. Thus this object could also be a WLQ with weak Mg II line emission (considering also the uncertain Mg II location due to the uncertainty from the photo- z). Therefore, 41–43 of the 44 selected quasars have spectroscopic confirmation.

Furthermore, we matched our selected 1591 quasars to the SDSS DR16 archival sources that are not included in our training process because they have $\text{zwarning} > 0$. This effort led to 5 additional objects that satisfy the criteria of spectral signal-to-noise ratios ≥ 3 within the observed wavelength range of 4000–7000 Å. We found clear and discernible broad emission lines in all 5 objects. These spectroscopic confirmations further validate the reliability of our selected quasars.

4. PHOTOMETRIC REDSHIFTS

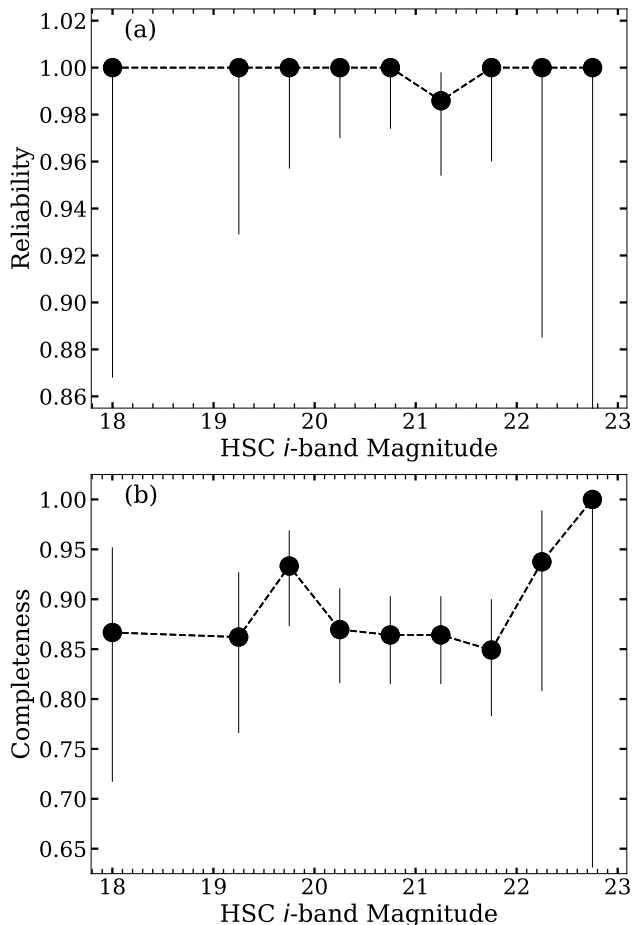


Figure 6. (a) Reliability versus observed *i*-band magnitude of the blind-test-sample quasars selected by XGBoost. (b) Completeness versus observed *i*-band magnitude of the blind-test sample quasars. The data are binned with a step of 0.5 magnitudes, except for those with $i < 19$, which are grouped into one bin. The errors are 1σ statistical uncertainties for individual bins (Gehrels 1986). There are no significant variations when considering the uncertainties.

To study the disk-corona connection, we require redshift information for our selected 1591 quasars. While spectroscopic redshifts (spec- z s) are ideal, a significant fraction ($\approx 40\%$) of them have no spec- z s. Therefore, we estimated photometric redshifts (photo- z s) for our selected quasars.

XGBoost offers a regression mode that can be utilized to estimate photo- z s. We constructed the training sample from the 1591 quasars in the XMM-SERVS XMM-LSS field, since the coverage of the VIDEO and CFHTLS surveys is more extensive. Among the 1591 quasars, 651 have SDSS $z_{\text{warning}} = 0$ spec- z s. For the 940 selected quasars without SDSS $z_{\text{warning}} = 0$ spec- z s, we collected spectroscopic redshifts from the redshift catalogs of other spectroscopic surveys, including the PRISM Multi-Object Survey (PRIMUS; Coil

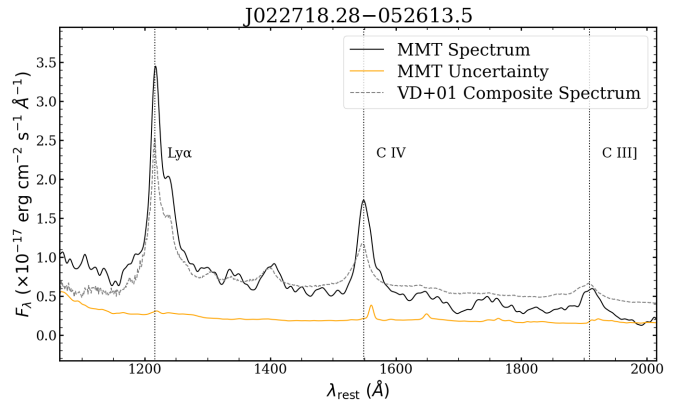


Figure 7. The MMT spectrum of J022718.28–052613.5 at $z_{\text{spec}} = 2.573$. The black and orange solid curves represent the flux and its uncertainty, respectively. We corrected the spectrum for the Galactic extinction. We smoothed the spectrum with a Gaussian kernel with a standard deviation of 10 pixels. We compared this spectrum to the composite quasar spectrum of Vanden Berk et al. (2001), which is represented as the dashed grey curve and normalized at rest-frame 1450 \AA . The photometric redshift predicted by the XGBoost model is 2.52.

et al. 2011), the 3D-HST Survey (Skelton et al. 2014; Momcheva et al. 2016) in the XMM-LSS field, the UKIDSS Ultra-Deep Survey (UDSz; Bradshaw et al. 2013, McLure et al. 2013), the VIMOS Public Extragalactic Redshift Survey (VIPERS; Garilli et al. 2014), and the VIMOS VLT Deep Survey (VVDS; Le Fèvre et al. 2013). Additionally, we used a compilation of publicly available but unpublished spec- z s in the UDS field (named as UDS Compilation in this study).⁹ We matched our quasars to the redshift catalogs of these surveys using a matching radius of $1''$ and obtained 371 quasars with matched spec- z s. For 71 of the 371 quasars with at least one secure spec- z (determined from multiple reliable spectral features with $\gtrsim 95\%$ confidence levels), we adopted their spec- z s in order of the VVDS, VIPERS, UDSz, and UDS Compilation catalogs, which are ranked by the spectral resolution at r band (Chen et al. 2018). Therefore, we obtained 722 (651 + 71) quasars with SDSS spec- z s or other secure spec- z s, and these quasars are utilized as the training sample for regression analysis. The spec- z s of the 722 quasars span a range of 0.127 to 3.860, with a median value of 1.574.

The regression model was trained using the same 18 colors that were utilized in our classification models (see Section 3.1). We fine-tuned the hyperparameters of the regression model through 5000 trials with OPTUNA. The

⁹ An overview of the redshift catalog can be found at <https://www.nottingham.ac.uk/astronomy/UDS/data/data.html>.

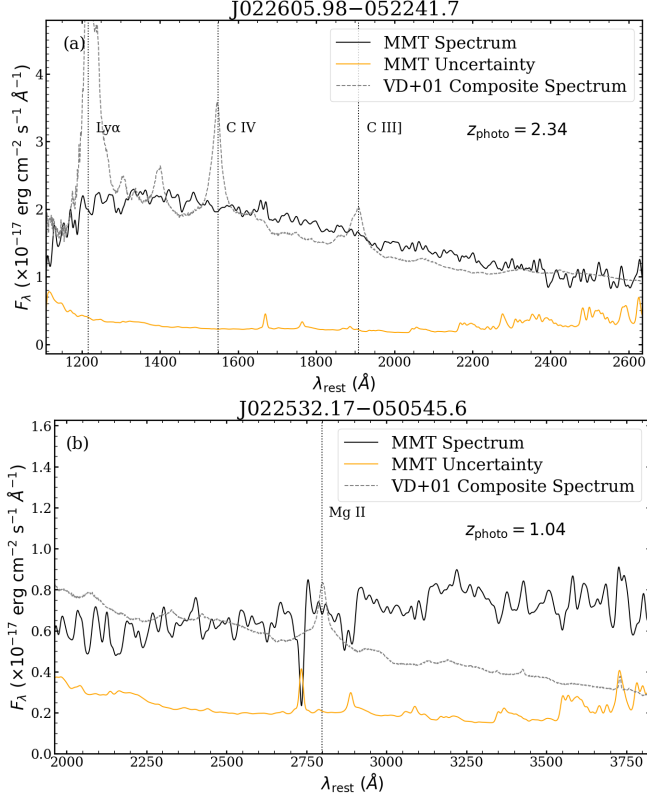


Figure 8. The MMT spectra of (a) J022605.98–052241.7 and (b) J022532.17–050545.6, plotted at their photo- z s of 2.34 and 1.04, respectively. There are no apparent broad emission lines in the two spectra. We compared these two spectra to the composite quasar spectrum from [Vanden Berk et al. \(2001\)](#), which is normalized at rest-frame 2500 Å. These two objects are probably weak emission-line quasars.

optimal model was selected based on the lowest mean square error (MSE)¹⁰ calculated from a five-fold cross validation of the training sample. The MSE of the five-fold cross validation of the training sample is 0.134. We also used two indicators to evaluate the photo- z quality, the outlier fraction (f_{outlier} ¹¹; e.g., [Hildebrandt et al. 2010](#), [Luo et al. 2010](#)) and the normalized median absolute deviation (NMAD) of Δz (σ_{NMAD} ¹²; e.g., [Ilbert et al. 2006](#), [Brammer et al. 2008](#)). The f_{outlier} and σ_{NMAD} values of the five-fold cross validation of the training sample are 18.4% and 0.054, respectively.

Subsequently, we used the optimized regression model to estimate the photo- z s of the entire set of 1591 photometrically selected quasars. The estimated photometric

¹⁰ $\text{MSE} = \frac{1}{N} \sum_{i=1}^N (z_{\text{spec}} - z_{\text{photo}})^2$.

¹¹ f_{outlier} is defined as the fraction of quasars with $|z_{\text{spec}} - z_{\text{photo}}| / (1 + z_{\text{spec}}) > 0.15$.

¹² $\sigma_{\text{NMAD}} = 1.48 \times \text{median}\left(\frac{|\Delta z - \text{median}(\Delta z)|}{1 + z_{\text{spec}}}\right)$, which is a robust indicator of the photo- z accuracy after the exclusion of outliers.

redshifts span a range of 0.41 to 3.75, with a median value of 1.64. We note that estimating photometric redshifts for type 1 quasars is challenging due to their typically power-law-shaped SEDs in the optical, resulting in colors that are rather independent of redshift (e.g., [Salvato et al. 2019](#)). To assess the performance of the optimal regressor, we also constructed a blind-test sample including 361 quasars outside the XMM-LSS field that also have SDSS `zwarning` = 0 spec- z s or other secure spec- z s. The blind-test sample is not used for training the regression model.

We applied the optimal regression model to the blind-test sample. Upon comparing the photo- z s and spec- z s of the blind-test sample, we obtained $\text{MSE} = 0.149$, $f_{\text{outlier}} = 22.7\%$, and $\sigma_{\text{NMAD}} = 0.079$. However, approximately 43% of the blind-test-sample quasars lacked CFHT u^* band photometry, whereas the fraction is only around 5% for the 1591 selected quasars in the XMM-LSS field. The u^* -band photometry of quasars is powerful for distinguishing between low and high photometric redshift solutions (e.g., [Salvato et al. 2019](#); [Sawicki et al. 2019](#)) and increasing the accuracy of photometric redshifts (e.g., [Yang et al. 2017](#)). Therefore, we checked the 211 blind-test-sample quasars that have CFHT u^* -band photometry, and we found that their photo- z s are more reliable, with $\text{MSE} = 0.111$, $f_{\text{outlier}} = 17.1\%$, and $\sigma_{\text{NMAD}} = 0.074$. The comparison between the photo- z s and spec- z s for these 211 quasars is illustrated in Figure 9. For the selected quasars in the XMM-LSS field with no SDSS `zwarning` = 0 spec- z s or other secure spec- z s, approximately 91% have CFHT u^* band photometry. Therefore, we estimated $f_{\text{outlier}} \approx 17\%$ and $\sigma_{\text{NMAD}} \approx 0.07$ for these selected quasars based on the photo- z accuracy of the blind-test-sample quasars with CFHT u^* -band photometry.

Our machine-learning-based photo- z quality is comparable to that of previous studies, which reported $f_{\text{outlier}} \approx 20\%$ (e.g., [Ni et al. 2021](#), [Li et al. 2022](#)). For comparison, we also utilized the Le PHARE SED-fitting code ([Arnouts et al. 1999](#); [Ilbert et al. 2006](#))¹³ to estimate the photo- z s for all the 1083 (722 + 361) quasars with SDSS `zwarning` = 0 spec- z s or other secure spec- z s in the training sample and blind-test sample. We utilized the SED library designed by [Salvato et al. \(2009\)](#), which contains 30 templates constructed for fitting SEDs of AGN-dominated sources. In our analysis, all the available 13-band photometric data for each quasar was utilized during the SED fitting. We adopted a minimum magnitude error of 0.06 for each band ([Luo et al. 2010](#))

¹³ <https://www.cfht.hawaii.edu/~arnouts/LEPHARE/lephare.html>.

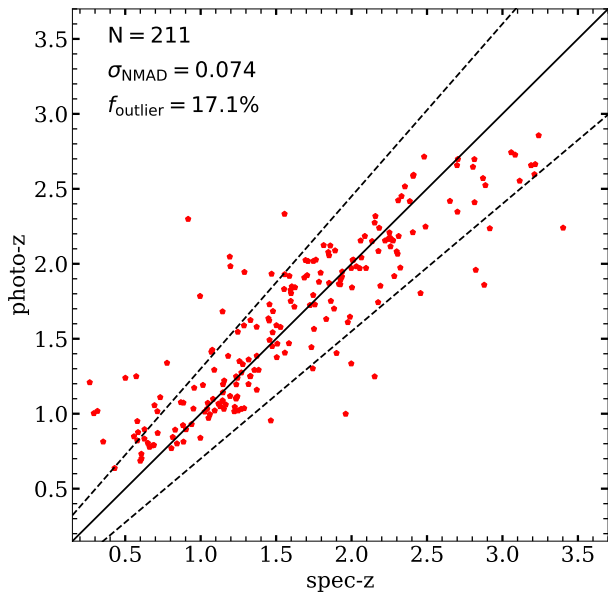


Figure 9. Comparison between the spectroscopic and the photometric redshifts for the 211 quasars with CFHT u^* -band photometry in the blind-test sample. The black solid line marks the $z_{\text{spec}} = z_{\text{phot}}$ relation. The black dashed lines are the $|\Delta z|/(1 + z_{\text{spec}}) = 0.15$ thresholds for outliers.

to reduce the influence of data points with unrealistically small errors. The photo- z results from Le PHARE, with $f_{\text{outlier}} = 29.5\%$ and $\sigma_{\text{NMAD}} = 0.072$, were less accurate than those from XGBoost.

Therefore, we adopt the XGBoost photo- z s in the following analyses. For the 300 quasars with insecure spec- z s (including spec- z s from PRIMUS and 3D-HST) and 35 quasars with only SDSS $z_{\text{warning}} > 0$ spec- z s, we adopted the spec- z if $|z_{\text{spec}} - z_{\text{photo}}|/(1 + z_{\text{spec}}) < 0.15$ (200 objects out of the 335); otherwise, the photo- z is adopted. Therefore, we have spec- z s for 922 (722 + 200) quasars and photo- z s for the remaining 669 quasars. We list the redshifts and the sources of redshift for our selected quasars in Table 4. In Figure 10, we display the absolute i -band magnitude at $z = 2$, $M_i(z = 2)$, versus the final adopted redshifts of the selected quasars. For each quasar, we calculated its $M_i(z = 2)$ value using the Galactic-extinction-corrected apparent i -band magnitude and the K correction from Table 4 of Richards et al. (2006).

5. DISK-CORONA CONNECTION

5.1. Exclusion of Radio-Loud Quasars

Radio-loud (RL) quasars may exhibit additional X-ray emission associated with jets or enhanced coronae (e.g.,

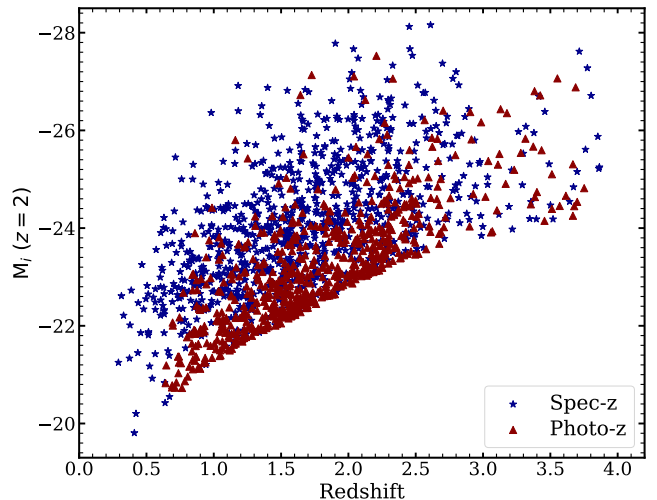


Figure 10. The absolute i -band magnitude at $z = 2$ vs. redshift for the 1591 selected quasars in the XMM-SERVS XMM-LSS field. The quasars with spec- z s or photo- z s are represented as the blue stars or the red triangles, respectively.

Miller et al. 2011; Zhu et al. 2020). We excluded RL quasars in our analysis of the disk-corona connection. The XMM-LSS field is fully covered by the Karl G. Jansky Very Large Array (VLA) survey (Heywood et al. 2020), and a fraction ($\gtrsim 50\%$) of it is covered by the MeerKAT International Gigahertz Tiered Extragalactic Explorations (MIGHTEE) survey (Heywood et al. 2022). We matched the 1591 quasars to the Zhu et al. (2023) source catalog using a matching radius of $1''$, which includes optical/IR sources in the XMM-SERVS fields with the MIGHTEE or VLA counterparts.

We identified 372 quasars with matched radio counterparts. For each of these quasars, we calculated the rest-frame 6 cm flux density ($f_{6\text{cm}}$) using the peak flux density of the corresponding radio counterpart and a power-law spectral slope of $a_r = -0.8$ (Falcke et al. 1996, Barvainis et al. 2005). In cases where a quasar lacks an associated radio counterpart, we estimated an upper limit on its radio flux density, which was set as 5 times the rms noise ($5\sigma_{\text{rms}}$) at the source position (Heywood et al. 2020, 2022). For each quasar, we determined the $f_{2500\text{\AA}}$ value and its associated $L_{2500\text{\AA}}$ value by interpolating or extrapolating its photometric data. Using these $f_{2500\text{\AA}}$ values and the $f_{6\text{cm}}$ values for each quasar, we computed the radio-loudness parameter (or its upper limit) as $R = f_{6\text{cm}}/f_{2500\text{\AA}}$ (e.g., Jiang et al. 2007). The R values (or their upper limits) for our quasars are detailed in Table 4. There are 123 quasars with R measurements exceeding 10, and they were classified as RL quasars (e.g., Kellermann et al. 1989; Jiang et al. 2007). Besides, 27 quasars with no radio counterparts were found to have R upper limits beyond 100, and

Table 4. Optical and X-ray Properties of Our Selected Quasars

RA	DEC	Redshift	Redshift	M_i ($z = 2$)	$f_{2500 \text{ \AA}}$	$f_{2 \text{ keV}}$	R	Γ_X	α_{OX}	$\Delta\alpha_{OX}$	$\alpha_{OX}-L_{2500 \text{ \AA}}$
(deg)	(deg)		Source								flag
(1)	(2)	(3)	(4)	(5)	(6)	(7)	(8)	(9)	(10)	(11)	(12)
34.2004	-4.9333	1.821	UDSz	-23.63	5.4	6.5	< 5.8	1.7	-1.50	-0.04	1
34.2012	-4.4987	1.178	SDSS	-23.15	7.3	4.1	13.4	1.7	-1.63	-0.20	0
34.2035	-5.6902	1.932	VIPERS	-23.55	4.8	13.5	< 73.7	1.7	-1.36	0.11	1
34.2053	-3.8765	2.08	XGB	-24.53	10.5	12.6	< 20.1	1.7	< -1.50	< 0.02	1
34.2083	-5.2951	1.280	UDS	-22.32	3.2	6.6	< 6.1	1.64	-1.41	-0.03	1
34.2092	-4.0285	1.031	SDSS	-23.37	11.2	27.0	< 6.2	1.13	-1.39	0.06	0
34.2180	-5.6016	1.439	SDSS	-23.09	5.7	10.3	< 24.6	1.0	-1.44	0.01	0
34.2195	-5.6841	2.612	SDSS	-26.04	28.2	21.6	< 15.1	1.7	-1.58	0.04	1
34.2206	-4.9130	1.622	UDS	-22.96	4.0	10.5	< 4.4	1.7	< -1.37	< 0.06	1
34.2233	-4.5127	1.636	SDSS	-24.56	17.1	5.4	< 1.6	1.7	-1.73	-0.19	1
34.2282	-4.9625	1.107	SDSS	-23.04	9.3	19.2	< 1.5	1.35	-1.41	0.03	1
34.2301	-5.1964	2.796	SDSS	-24.88	9.2	5.6	< 2.9	1.7	-1.62	-0.06	1
34.2305	-5.3933	2.221	SDSS	-24.30	7.6	11.9	< 3.8	1.53	-1.46	0.05	1
34.2356	-5.5001	0.69	XGB	-20.78	1.3	8.6	266.1	1.7	< -1.22	< 0.02	0
34.2398	-4.0789	1.738	SDSS	-23.30	5.4	14.9	< 13.2	1.79	-1.37	0.10	1
34.2420	-5.5805	2.31	XGB	-24.84	10.8	18.7	< 14.8	1.7	< -1.44	< 0.10	1
34.2452	-4.2861	2.089	PRIMUS	-24.07	6.9	7.3	< 5.0	1.7	-1.53	-0.02	1
34.2463	-4.7591	1.071	SDSS	-23.08	10.8	15.4	< 1.7	1.97	-1.48	-0.03	1
34.2472	-5.4082	1.426	SDSS	-22.90	5.2	7.4	12.6	1.7	-1.48	-0.04	0

NOTE— Columns (1)-(2): the HSC right ascension and declination (in degrees) of the selected quasar. Column (3): the redshift. Column (4): the source of redshift; photo-zs are labeled as “XGB”. Column (5): the absolute i -band magnitude at $z = 2$. Column (6): the rest-frame 2500 Å flux density in units of $10^{-29} \text{ erg cm}^{-2} \text{ s}^{-1} \text{ Hz}^{-1}$. Column (7): the rest-frame 2 keV flux density or its 3σ upper limit in units of $10^{-33} \text{ erg cm}^{-2} \text{ s}^{-1} \text{ Hz}^{-1}$. Column (8): the radio loudness parameters. Column (9): the effective photon index, set as “1.7” if the quasar is not detected in the hard band (including quasars with no X-ray detection); or “1.0” if the quasar is detected in the hard band but not the soft band. Column (10): the measured α_{OX} parameter. Column (11): the difference between the measured α_{OX} and the expected α_{OX} from Equation 4. Column (12): a flag of “1” indicates that the quasar is used for deriving the disk-corona correlation (Equation 4). The full table contains the optical and X-ray properties of our 1591 quasars selected by XGBoost in the XMM-SERVS XMM-LSS field. Only a portion of this table is shown here to demonstrate its form and content.

(This table is available in its entirety in machine-readable form.)

Table 5. Step-by-step Construction of the Subsample

Selection Criteria	Number of Quasars
In parent sample, selected by XGBoost	2784
In XMM-LSS field	1591 (Table 4)
Excluding 150 RL quasars	1441
$i < 22.5$	1132
Excluding 116 X-ray-absorbed quasars	1016 (Figure 13) (including 275 X-ray-undetected)

we consider them as RL quasar candidates in this study. All these 150 (123+27) quasars were excluded from the analysis of the $\alpha_{OX}-L_{2500 \text{ \AA}}$ relation below. We still derived the X-ray properties of these 150 quasars following the approach in Section 5.2 below, and these are also listed in Table 4.

5.2. X-ray Properties and Subsample Construction

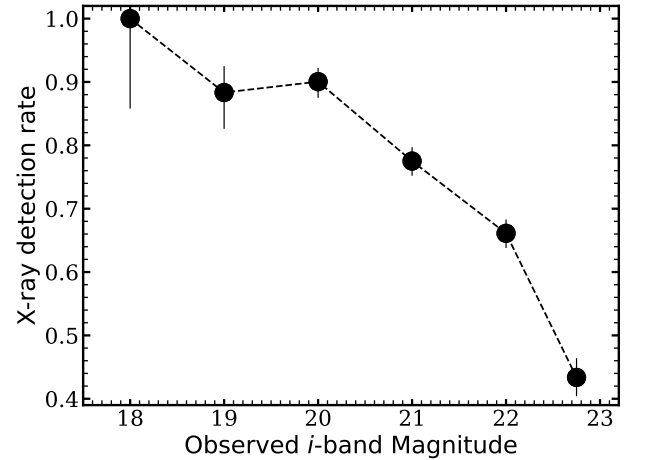


Figure 11. The X-ray detection rate vs. observed i -band magnitude of the 1441 selected quasars. Data are binned with a step of 1 magnitude, spanning the range from 17.5 to 22.5. The errors are 1σ statistical uncertainties. The detection rate drops as the magnitude increases.

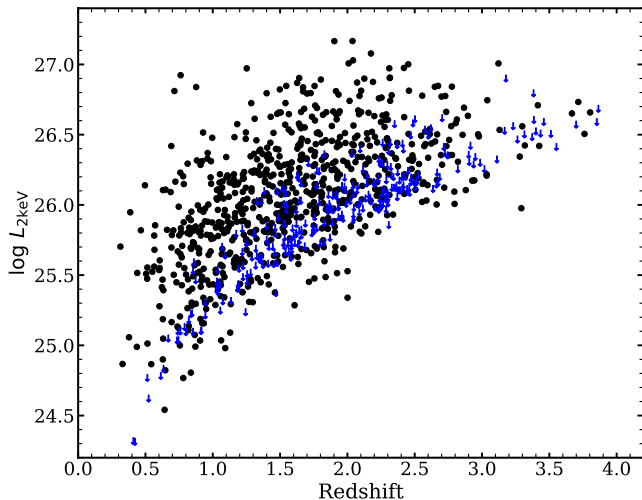


Figure 12. The distribution of $L_{2 \text{ keV}}$ vs. redshifts for the 1016 subsample of quasars. The 3σ $L_{2 \text{ keV}}$ upper limits of those quasars with no X-ray detection, calculated from the soft-band sensitivity map, are marked as blue arrows.

To obtain the X-ray properties of our selected quasars, we matched the X-ray sources (using the coordinates of their optical-to-NIR counterparts) in the catalog of Chen et al. (2018) to our 1441 radio-quiet (RQ) quasars (using the HSC coordinates) with an $1''$ matching radius. A quasar is considered X-ray-detected if it has a matched X-ray counterpart. We obtained 991 matches ($\approx 69\%$), and we show the relationship between the X-ray detection rate and the i -band magnitude of the 1441 quasars in Figure 11. The X-ray detection rate decreases as the objects become optically fainter, likely due to the survey sensitivity limitation. More than half of the quasars with $22.5 < i < 23$ are not detected.

We computed the $f_{2 \text{ keV}}$ values for the X-ray-detected RQ quasars from their count rates and fluxes in the Chen et al. (2018) catalog:

1. For the quasars that are detected in both the soft (0.5–2 keV) and hard (2–10 keV) X-ray bands, we estimated their X-ray effective power-law photon indices (Γ_{eff}) from their soft-to-hard-band ratios, calculated using their two-band count rates of the pn camera (Strüder et al. 2001) provided by the Chen et al. (2018) catalog. We adopted a typical pn response file and a simple power-law model modified by Galactic absorption ($N_{\text{H}} = 3.57 \times 10^{20} \text{ cm}^{-2}$; HI4PI Collaboration et al. 2016) to determine the Γ_{eff} values. We calculated the $f_{2 \text{ keV}}$ values from their soft-band fluxes using their estimated Γ_{eff} values.
2. For the quasars that are detected in the soft band but not the hard band, we assumed $\Gamma_{\text{eff}} = 1.7$,

which is adopted in Chen et al. (2018). We then calculated their $f_{2 \text{ keV}}$ values from their soft-band fluxes.

3. For the other quasars that are detected in the hard band but not the soft band (they are all detected in the full band), we assumed $\Gamma_{\text{eff}} = 1.0$ and calculated the $f_{2 \text{ keV}}$ values from their full-band fluxes. We caution that this Γ_{eff} value is arbitrarily chosen and the actual spectral shape (and subsequently the $f_{2 \text{ keV}}$ value) might be off by a large amount. These quasars are not included in our study of the $\alpha_{\text{OX}}-L_{2500 \text{ \AA}}$ relation below as they are considered likely to be X-ray absorbed. Any future citations to these $f_{2 \text{ keV}}$ values should be treated with caution.

For the other quasars that are not X-ray-detected, we first derived the 3σ upper limits on their soft-band fluxes from the survey sensitivity using Equation 3 of Chen et al. (2018). We then estimated the 3σ upper limit on $f_{2 \text{ keV}}$ by assuming an X-ray power-law photon index of 1.7. In Figure 12, we present the distribution of $L_{2 \text{ keV}}$ values versus redshifts for our subsample of quasars. We list the Γ_{eff} and $f_{2 \text{ keV}}$ values of the 1441 quasars in Table 4.

To construct a subsample of quasars with a high X-ray detection rate for the analysis of the $\alpha_{\text{OX}}-L_{2500 \text{ \AA}}$ relation (Section 5.3 below), we first considered only the 1132 RQ quasars with $i < 22.5$. Among these, 857 quasars have matched X-ray counterparts ($\approx 75\%$). We then excluded quasars that are probably X-ray-absorbed from our analysis, as the X-ray emission does not represent the intrinsic coronal emission. This exclusion is important to mitigate potential biases when studying the connection between the accretion disk and the corona. We adopted a criterion of $\Gamma_{\text{eff}} < 1.26$ that was previously adopted by Pu et al. (2020) and excluded 116 quasars.¹⁴ We caution that among the X-ray undetected quasars there should also be X-ray absorbed ones. This potential bias is discussed in Section 5.4.1 below. The final subsample for studying the quasar disk-corona connection contains 1016 quasars. The step-by-step construction of our subsample is listed in Table 5 for clarity.

5.3. The $\alpha_{\text{OX}}-L_{2500 \text{ \AA}}$ Correlation

Using the $f_{2 \text{ keV}}$ values or upper limits in conjunction with the $f_{2500 \text{ \AA}}$ values, we calculated the α_{OX} values

¹⁴ We have also explored alternative Γ_{eff} thresholds of 1.0, 1.1, 1.2, and 1.4, and we found that all the derived correlations between α_{OX} and $L_{2500 \text{ \AA}}$ are consistent with each other within the 1σ uncertainties.

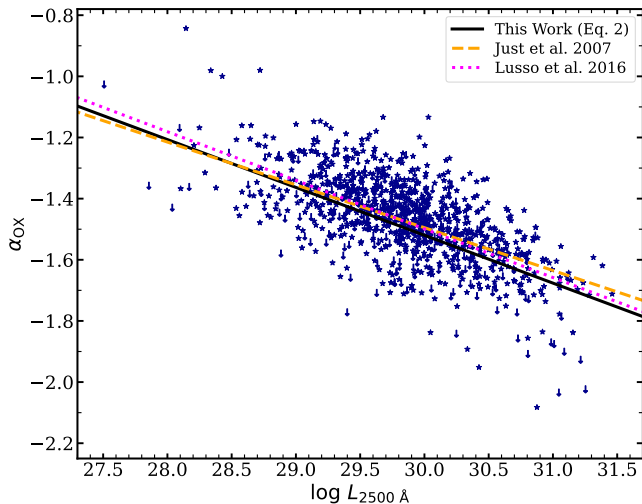


Figure 13. The distribution of α_{OX} vs. $L_{2500 \text{ \AA}}$ values for our 1016 subsample of quasars. Those quasars with no X-ray detection are marked as arrows. Our $\alpha_{\text{OX}}-L_{2500 \text{ \AA}}$ relation is represented by the black solid line, while the $\alpha_{\text{OX}}-L_{2500 \text{ \AA}}$ correlations of Just et al. (2007) and Lusso & Risaliti (2016) are represented as orange dashed line and magenta dotted line for comparison. Our $\alpha_{\text{OX}}-L_{2500 \text{ \AA}}$ relation is in good agreement with the two correlations considering the uncertainties.

or upper limits for our subsample of 1016 quasars, including 741 detections and 275 upper limits. To examine the $\alpha_{\text{OX}}-L_{2500 \text{ \AA}}$ relation, we utilized the Astronomy Survival Analysis package (ASURV Rev 1.2; Isobe & Feigelson 1990; Lavalley et al. 1992), which is capable of handling censored data. We confirm a significant anti-correlation (at an $\approx 17.7\sigma$ level) between α_{OX} and $L_{2500 \text{ \AA}}$ through the generalized Kendall’s τ test available in ASURV. We utilized the EM (estimate and maximize) algorithm in ASURV to determine the linear regression parameters. In Figure 13, we display the derived correlation and the distribution of α_{OX} versus $L_{2500 \text{ \AA}}$. The derived correlation for our subsample of quasars is

$$\alpha_{\text{OX}} = (-0.156 \pm 0.007) \log L_{2500 \text{ \AA}} + (3.175 \pm 0.211). \quad (4)$$

The dispersion of the correlation is calculated as the rms of $\Delta\alpha_{\text{OX}}$ ¹⁵ obtained from the Kaplan-Meier estimator in ASURV, which is 0.159. For each quasar, we list its α_{OX} and $\Delta\alpha_{\text{OX}}$ values in Table 4.

We compared our results to those in two previous studies which also used optically selected AGNs and censored data to study the AGN $\alpha_{\text{OX}}-L_{2500 \text{ \AA}}$ relation,

¹⁵ $\Delta\alpha_{\text{OX}} = \alpha_{\text{OX}} - \alpha_{\text{OX, exp}}$, where α_{OX} is the measured value, and $\alpha_{\text{OX, exp}}$ is the expected value derived from Equation 4.

Just et al. (2007) and Lusso & Risaliti (2016). We first compared the numbers of quasars and the $\log L_{2500 \text{ \AA}}$ and z ranges. Just et al. (2007) constructed their composite sample, totaling 372 AGNs, by combining the Strateva et al. (2005) AGN sample (most of which are SDSS DR2 AGNs, plus a low-redshift Seyfert 1 sample from Walter & Fink 1993), photometrically selected COMBO-17 AGNs (Wolf et al. 2004), and a subsample of high-luminosity quasars (Schmidt & Green 1983; Vignali et al. 2005). They obtained the X-ray properties from several observatories. The main sample of Lusso & Risaliti (2016) consists of 2685 SDSS DR7 quasars from Shen et al. (2011), with X-ray properties obtained from the 3XMM-DR5 source catalog (Rosen et al. 2016). Our subsample includes a larger number of quasars compared to Just et al. (2007). The number of quasars identified could potentially double if our method is applied to the other two XMM-SERVS fields. The low-luminosity end of the 90% $\log L_{2500 \text{ \AA}}$ range (from 28.87 to 30.80) of our subsample of quasars is ≈ 0.3 dex higher than that in Just et al. (2007) (28.87 vs. 28.56) and ≈ 0.4 dex lower than that in Lusso & Risaliti (2016) (28.87 vs. 29.31), benefiting from our machine-learning quasar selection approach. Therefore, we consider that our method can systematically select a large number of quasars while extending the luminosity range to the low-luminosity end. We then compared the $\alpha_{\text{OX}}-L_{2500 \text{ \AA}}$ relations. Both Just et al. (2007) and Lusso & Risaliti (2016) used ASURV for deriving their $\alpha_{\text{OX}}-L_{2500 \text{ \AA}}$ relations. In Figure 13, we compare Equation 4 to the correlations obtained by Just et al. (2007) and Lusso & Risaliti (2016). Notably, Equation 4 shows good agreement with the correlations reported in both studies. We also calculated the correlation dispersion of Just et al. (2007) and Lusso & Risaliti (2016) by using the Kaplan-Meier estimator within ASURV, which are 0.173 and 0.207, respectively. The dispersion (0.159) of our correlation is slightly smaller than those of Just et al. (2007) and Lusso & Risaliti (2016).

We also compared our result to that in Lusso et al. (2020), whose sample contains 2421 optically selected quasars with spectroscopic redshifts and X-ray detections from either Chandra or XMM-Newton. Lusso et al. (2020) selected quasars that are neither reddened by dust in the optical/UV nor obscured by gas in the X-ray, and the X-ray fluxes are free from flux-limit related biases. Our subsample has a low-luminosity end of the 90% $\log L_{2500 \text{ \AA}}$ range ≈ 0.3 dex lower than that in Lusso et al. (2020) (28.87 vs. 29.22). Lusso et al. (2020) did not derive the $\alpha_{\text{OX}}-L_{2500 \text{ \AA}}$ relation in their study. Using their data, we used ASURV to obtain the $\alpha_{\text{OX}}-L_{2500 \text{ \AA}}$ relation for the 2421 quasars. The relation

slope and intercept are -0.154 ± 0.003 and 3.139 ± 0.098 , respectively, and these are in good agreement with those of Equation 4 within the 1σ uncertainties. The relation has a significantly smaller dispersion of 0.098 compared to Equation 4 and those of Just et al. (2007) and Lusso & Risaliti (2016), which is likely benefiting from using only X-ray-detected quasars (see 5.4.1).

5.4. Potential Effects that May Bias the $\alpha_{\text{OX}}-L_{2500 \text{ \AA}}$ Relation

5.4.1. Effects from Potentially X-ray-absorbed Quasars

We note that 275 quasars in our subsample are not X-ray detected. Given the good sensitivity of the XMM-SERVS survey compared to the brightness cut of our sample construction (Point 2 of Section 2.2), it is unlikely that the nondetections were mainly caused by limited X-ray sensitivity. Instead, a substantial fraction of these X-ray undetected quasars should exhibit weak X-ray emission. For instance, assuming $\Gamma_{\text{eff}} = 1.7$ and the $f_{2 \text{ keV}}$ values expected from Equation 4, we estimated that 253 (76) of these X-ray undetected quasars should have soft-band fluxes exceeding the soft-band limiting fluxes (three times the limiting fluxes) if they produce a nominal amount of X-ray emission ($\Delta\alpha_{\text{OX}} = 0$).¹⁶ Such X-ray weak quasars might include broad absorption line (BAL) quasars (e.g., Gallagher et al. 2002, 2006; Fan et al. 2009; Gibson et al. 2009), weak-line quasars (e.g., Luo et al. 2015; Ni et al. 2018, 2022; Timlin et al. 2020b), and red quasars (e.g., Hall et al. 2006; Pu et al. 2020), and the X-ray weakness in these quasars is often ascribed to X-ray absorption. Therefore, besides the excluded quasars with $\Gamma_{\text{eff}} < 1.26$ (see Section 5.2), some of these undetected quasars are probably also X-ray-absorbed. The inclusion of these potentially X-ray-absorbed quasars might bias the $\alpha_{\text{OX}}-L_{2500 \text{ \AA}}$ relation.

We thus performed an analysis of the $\alpha_{\text{OX}}-L_{2500 \text{ \AA}}$ relation using only the 741 X-ray-detected quasars. In this subset, we found a correlation slope of 0.157 ± 0.007 , a correlation intercept of 3.237 ± 0.198 , and a dispersion of 0.109. While the new correlation intercept is larger than that of Equation 4, both the new correlation slope and intercept are consistent with those in Equation 4 within the 1σ uncertainties. This suggests that these potentially X-ray-absorbed quasars do not significantly affect the shape of the $\alpha_{\text{OX}}-L_{2500 \text{ \AA}}$ relation (e.g., Lusso

& Risaliti 2016; Lusso et al. 2020; Timlin et al. 2020b). Moreover, the dispersion is reduced compared to Equation 4, which is also found in previous studies (e.g., Lusso & Risaliti 2016).

5.4.2. Effects from Host-galaxy Contamination and Dust Extinction

We note that there are no constraints on the estimation of the $L_{2500 \text{ \AA}}$ values of our subsample of quasars. However, host-galaxy contamination and dust extinction may both contribute to the reddening of the optical/UV continua of quasars, resulting in overestimation or underestimation of the $L_{2500 \text{ \AA}}$ values, respectively. To assess the reddening effects, we tested to isolate a sample of quasars with little UV reddening.

For each quasar in our subsample, we calculated its observed UV power-law spectral slope at rest-frame wavelength of 2500 Å, denoted as α_{ν} ($f_{\nu} \propto \nu^{\alpha_{\nu}}$). To derive this spectral slope, we utilized interpolation or extrapolation based on the closest photometric measurements to the quasar’s rest-frame 2500 Å. We then computed the $\alpha_{\nu, 2500 \text{ \AA}}$ value for a reddened quasar SED template. Specifically, we used composite #29 in Salvato et al. (2009), and we modeled the reddened template SED by utilizing the extinction curve of the Small Magellanic Cloud (SMC; Gordon et al. 2003) with an extinction value of $E(B - V) = 0.15$. Such an $E(B - V)$ value indicates a change of ≈ 0.1 in the $\Delta\alpha_{\text{OX}}$ value. We then convolved the reddened SED to flux densities with the filter transmission curve corresponding to the two bands we used to derive the observed $\alpha_{\nu, 2500 \text{ \AA}}$ value. From the flux densities, we calculated the $\alpha_{\nu, 2500 \text{ \AA}}$ value of the reddened template SED.

Out of the 1016 quasars in our subsample, we found that 832 quasars have observed $\alpha_{\nu, 2500 \text{ \AA}}$ values that are larger than that calculated from the reddened template SED. These 832 quasars are likely not significantly affected by host-galaxy contamination or dust extinction. The average $\log L_{2500 \text{ \AA}}$ of the other 184 quasars is 29.4, which is 0.5 dex lower than that of the 832 quasars (29.9). We analyzed the $\alpha_{\text{OX}}-L_{2500 \text{ \AA}}$ relation for these 832 quasars, and we found that the result closely resembles Equation 4, with a correlation slope of -0.155 ± 0.008 , an intercept of 3.124 ± 0.246 , and a dispersion of 0.144. This result is consistent with findings from previous studies (e.g., Lusso et al. 2010; Lusso & Risaliti 2016; Chiaraluze et al. 2018), which suggest that host-galaxy contamination and dust extinction do not have significant effects on the derived $\alpha_{\text{OX}}-L_{2500 \text{ \AA}}$ relation for type 1 quasars. Additionally, the slightly smaller dispersion (0.144) compared to that (0.159) of Equation 4 suggests that the exclusion of quasars affected by significant UV reddening has the potential

¹⁶ The X-ray weakness of an undetected quasar is generally not reflected by its $\Delta\alpha_{\text{OX}}$ upper limit as we used stringent 3σ upper limits. For example, for a quasar having expected $f_{2 \text{ keV}}$ three times above the sensitivity limit, its $\Delta\alpha_{\text{OX}}$ upper limit is ≈ -0.05 .

to reduce the dispersion of $\alpha_{\text{OX}}-L_{2500 \text{ \AA}}$ relation (e.g., Chiaraluce et al. 2018).

5.4.3. Effects from Extreme X-ray Variability

Previous studies suggested that non-simultaneous UV and X-ray measurements has limited effects on the scatter of the $\alpha_{\text{OX}}-L_{2500 \text{ \AA}}$ relation, with the intrinsic variability of α_{OX} values of individual quasars contributing $\approx 40 - 60\%$ of the dispersion (e.g., Vagnetti et al. 2010, 2013; Chiaraluce et al. 2018). The typical X-ray flux variability amplitudes for RQ type 1 quasars range from $\approx 20\%$ to 50% , which is generally ascribed to instability/fluctuation of the accretion disk and corona (e.g., McHardy et al. 2006; MacLeod et al. 2010; Yang et al. 2016; Zheng et al. 2017). Besides the stochastic coronal variability, a number of type 1, RQ, and non-BAL quasars have been found to exhibit extreme and sometimes rapid (down to hours) X-ray variability with large variation amplitudes (factors of $\gtrsim 10$; e.g., PHL 1092, Miniutti et al. 2012; SDSS J075101.42+291419.1, Liu et al. 2019; SDSS J153913.47+395423.4, Ni et al. 2020; SDSS J135058.12+261855.2, Liu et al. 2022; SDSS J081456.10+532533.5, Huang et al. 2023; SDSS J142339.87+042041.1, Zhang et al. 2023; SDSS J152156.48+520238.5, Wang et al. 2024). Their optical/UV and IR variability during the same period remains limited, suggesting no significant changes in accretion rates. One possible explanation for such variability is varying obscuration from clumpy accretion-disk winds (e.g., Liu et al. 2022; Wang et al. 2022; Huang et al. 2023). In this case, only the high-state X-ray emission of these quasars may represent the unabsorbed, intrinsic coronal emission, and studies of their intrinsic disk-corona connection should be based on high-state X-ray properties. For example, Liu et al. (2021) studied the $\alpha_{\text{OX}}-L_{2500 \text{ \AA}}$ relation for a sample of AGNs by using only high-state X-ray data, and most of the AGNs have simultaneous UV measurements. They found a smaller dispersion (≈ 0.07) of the $\alpha_{\text{OX}}-L_{2500 \text{ \AA}}$ relation compared to previous studies.

In our study, while the selection of quasars with $\Gamma_{\text{eff}} > 1.26$ helps us to obtain the high-state X-ray properties, sometimes the low-state X-ray spectra dominated by leaked X-ray emission may also show large Γ values (e.g., Liu et al. 2019; Wang et al. 2022; Huang et al. 2023). Therefore, we checked whether there are such quasars with extreme X-ray variability in our subsample. Based on the analysis of the X-ray variability of 4XMM-DR13 catalog (Webb et al. 2020; Traulsen et al. 2020) sources in the XMM-SERVS XMM-LSS field, Zhang Z.J. et al (submitted) discovered 8 AGNs with X-ray variation amplitude ranging from 6 to 12, and only 3 of these

are in our subsample. This result is consistent with the low occurrence rate ($\lesssim 1 - 4\%$) of quasar extreme X-ray variability (e.g., Gibson & Brandt 2012; Timlin et al. 2020a). Therefore, the limited number of quasars in our subsample exhibiting extreme X-ray variability suggests that their effects on our $\alpha_{\text{OX}}-L_{2500 \text{ \AA}}$ relation is likely not significant.

5.5. Evolution with $L_{2500 \text{ \AA}}$ or z ?

Previous studies have suggested possible evolution of the $\alpha_{\text{OX}}-L_{2500 \text{ \AA}}$ relation with respect to $L_{2500 \text{ \AA}}$ or redshift, as the relation slope for high- $L_{2500 \text{ \AA}}$ or high- z quasars appears steeper (e.g., Steffen et al. 2006; Gibson et al. 2008; Chiaraluce et al. 2018; Pu et al. 2020; Timlin et al. 2020b). For example, Pu et al. (2020) studied the $\alpha_{\text{OX}}-L_{2500 \text{ \AA}}$ relation for a sample of high- $L_{2500 \text{ \AA}}$ SDSS quasars with a 90% log $L_{2500 \text{ \AA}}$ range from 29.9 to 31.2, and they found a much steeper relation slope of -0.224 ± 0.008 , which differs from Equation 4 (-0.156 ± 0.007) at an $\approx 6.7\sigma$ level. To investigate whether such an evolution is present in our subsample of quasars, we selected a subset of 211 high- $L_{2500 \text{ \AA}}$ SDSS quasars from our subsample by adopting the same redshift ($1.7 < z < 2.7$) criterion that was used in Pu et al. (2020). The 90% log $L_{2500 \text{ \AA}}$ range of these 211 quasars is from 29.8 to 31.0, comparable to that of Pu et al. (2020). We then used ASURV to derive the $\alpha_{\text{OX}}-L_{2500 \text{ \AA}}$ relation for the 212 quasars. The relation slope and intercept are -0.191 ± 0.020 and 4.256 ± 0.594 , respectively. Despite the significance of difference being only at an $\approx 1.7\sigma$ level, the new relation slope is steeper compared to that of Equation 4. The significance of this trend for our quasars is low due to the limited number of $1.7 < z < 2.7$ SDSS quasars. We also divided all of our subsample of quasars into two groups using $z = 1.7$ as a threshold. The median values of $L_{2500 \text{ \AA}}$ for the $z < 1.7$ (low- $L_{2500 \text{ \AA}}$) and $z > 1.7$ (high- $L_{2500 \text{ \AA}}$) groups are 29.5 and 30.1, respectively. The $\alpha_{\text{OX}}-L_{2500 \text{ \AA}}$ relation slopes for the two groups are -0.144 ± 0.011 and -0.182 ± 0.013 , respectively. The evolutionary trend still exists as the two relation slopes differ at an $\approx 2.2\sigma$ level. We note it is difficult to disentangle the degeneracy between $L_{2500 \text{ \AA}}$ and z for a flux limited quasar sample, and thus the evolution may be related to either of these.

We further tested this possible evolution of the $\alpha_{\text{OX}}-L_{2500 \text{ \AA}}$ relation with respect to $L_{2500 \text{ \AA}}/z$ using the quasars from Lusso & Risaliti (2016) and Lusso et al. (2020). We selected the $1.7 < z < 2.7$ quasars from Lusso & Risaliti (2016) and Lusso et al. (2020) and derived the corresponding $\alpha_{\text{OX}}-L_{2500 \text{ \AA}}$ relations using ASURV. The new relation slopes for Lusso & Risaliti (2016) and Lusso et al. (2020) are -0.228 ± 0.013

and -0.181 ± 0.007 , respectively. Compared to the relation slopes for their full samples (0.159 ± 0.005 and 0.154 ± 0.003), the differences are at $\approx 4.9\sigma$ and $\approx 3.2\sigma$ levels, respectively.

Therefore, our analyses suggest that the $\alpha_{\text{OX}}-L_{2500 \text{ \AA}}$ relation exhibits an evolution where the correlation becomes steeper in the high- $L_{2500 \text{ \AA}}$ /high- z regime. This evolution might be driven by the dependence of α_{OX} on more fundamental parameters of SMBH such as $L_{\text{Bol}}/L_{\text{Edd}}$ and M_{BH} (e.g., Shemmer et al. 2008; Lusso et al. 2010; Chiaraluce et al. 2018; Liu et al. 2021). For example, Liu et al. (2021) proposed that $\alpha_{\text{OX}} = -0.13 \log(L_{\text{Bol}}/L_{\text{Edd}}) - 0.10 \log M_{\text{BH}} - 0.69$, based on a sample of 47 AGNs with reverberation mapping measured M_{BH} values. Such different coefficients on the $L_{\text{Bol}}/L_{\text{Edd}}$ and M_{BH} parameters would lead to different $\alpha_{\text{OX}}-L_{2500 \text{ \AA}}$ relations for samples with different $L_{\text{Bol}}/L_{\text{Edd}}$ and M_{BH} distributions. However, L_{Bol} and M_{BH} estimates for typical quasars have large uncertainties, and it is not even clear that the α_{OX} versus $L_{\text{Bol}}/L_{\text{Edd}} + M_{\text{BH}}$ dependence is more fundamental than the α_{OX} versus $L_{2500 \text{ \AA}}$ dependence (e.g., Chiaraluce et al. 2018; Liu et al. 2021). Therefore, future larger quasar samples with well-estimated L_{Bol} and M_{BH} are needed to reveal the nature of the $\alpha_{\text{OX}}-L_{2500 \text{ \AA}}$ relation.

6. CONCLUSION AND FUTURE WORK

In this study, we have selected a sample of quasars located in the XMM-LSS field using a machine-learning approach. Our primary objective is to investigate the disk-corona connection in these quasars. We summarize our study as follows:

1. We constructed a parent sample comprising 168 805 sources that were detected in the HSC g , r , i , z , and y bands, as well as the Spitzer Deep-Drill IRAC 3.6 μm and 4.5 μm bands. We then matched the CFHTLS, GALEX, and VIDEO catalog sources to our parent sample to retrieve available photometric data from these surveys. See Section 2.2 and Section 2.3.
2. We have created both training and blind-test samples by extracting SDSS spectroscopically identified type 1 quasars, galaxies, and stars from our parent sample. The training sample is confined to the XMM-LSS field, while the blind-test sample extends beyond this region. See Section 2.4 and Section 2.5.
3. We utilized the XGBoost algorithm, trained using the training sample, to select a total of 1591 quasars from the parent-sample sources located

within the XMM-SERVS XMM-LSS field. We assessed its classification performance based on the blind-test sample. The outcome was favorable, demonstrating high reliability (approximately 99%) and good completeness (approximately 90%). See Section 3.

4. We used XGBoost to estimate the photometric redshifts of our quasars. The training sample comprises the photometrically selected quasars with SDSS or other secure spec- z s in the XMM-LSS field. The accuracy of these photometric redshift estimates is acceptable, with $f_{\text{outlier}} \approx 17\%$ and $\sigma_{\text{NMAD}} \approx 0.07$. Furthermore, we gathered spectroscopic redshift data from various survey catalogs for our quasars. See Section 4.
5. We matched the selected quasars to the X-ray source catalog of Chen et al. (2018). We utilized the measurements available in the X-ray source catalog to calculate the X-ray properties of the quasars. For quasars that were X-ray undetected, we computed the 3σ upper limit on $f_{2 \text{ keV}}$ using the soft-band sensitivity map constructed by Chen et al. (2018). See Section 5.2.
6. We studied the $\alpha_{\text{OX}}-L_{2500 \text{ \AA}}$ relation for a subsample consisting of 1016 RQ quasars where quasars with possible X-ray absorption were excluded. See Sections 5.1 and 5.2. Our derived correlation (Equation 4) has a correlation slope of (-0.156 ± 0.007) , an intercept of (3.175 ± 0.210) , and a dispersion of 0.159. The correlation is in good agreement with those in Lusso & Risaliti (2016) and Just et al. (2007). See Section 5.3.
7. We explored several factors that may bias the $\alpha_{\text{OX}}-L_{2500 \text{ \AA}}$ relation, including potentially X-ray-absorbed quasars, UV reddening, and extreme X-ray variability. We found no significant effects from these factors on the derived $\alpha_{\text{OX}}-L_{2500 \text{ \AA}}$ relation. See Section 5.4.
8. Consistent with previous studies, we identified an evolutionary trend of the $\alpha_{\text{OX}}-L_{2500 \text{ \AA}}$ relation for our subsample of quasars, where it becomes steeper in the higher $L_{2500 \text{ \AA}}/z$ regime. This trend is also apparent from our analyses of the quasars in Lusso & Risaliti (2016) and Lusso et al. (2020). See Section 5.5.

Our future studies will focus on the other two XMM-SERVS regions, the $\approx 4.6 \text{ deg}^2$ W-CDF-S and $\approx 3.2 \text{ deg}^2$ ELAIS-S1 regions, where the XMM-Newton

source catalogs are presented in Ni et al. (2021). Both of these two regions are covered by HSC and DeepDrill surveys, similar to the XMM-LSS field. We intend to utilize our quasar selection methods on the photometric sample sources within these two regions to obtain a larger sample of quasars, enabling us to better investigate the connection between the accretion disk and the corona. Forthcoming spectroscopic data in the XMM-SERVS regions from instruments such as the Prime Focus Spectrograph (e.g., Greene et al. 2022), Multi-Object Optical and Near-infrared Spectrograph (e.g., Maiolino et al. 2020), and 4-metre Multi-Object Spectroscopic Telescope (Swann et al. 2019) will provide a larger training sample and better redshift measurements which should benefit greatly the photometric selection of quasars and study of the $\alpha_{\text{OX}}-L_{2500 \text{ \AA}}$ relation.

This study may also be applicable to the forthcoming large samples of photometric quasars selected from the wide-field multiband imaging and spectroscopic survey of the Chinese Space Station Telescope (CSST; Zhan 2011). The CSST wide-field multiband imaging survey is aimed to image approximately 17 500 square degrees of the sky using NUV, u , g , r , i , z , and y bands, achieving a 5σ limiting magnitude of 25.4 (AB mag) or higher for point sources in the NUV and u bands. The CSST wide-field slitless spectroscopic survey will also cover approximately 17 500 square degrees of the sky using GU, GV, and GI bands, achieving a 5σ limiting magnitude of 23.2 (AB mag) or higher for point sources in the GU bands. Combining the CSST imaging survey with future deep IR surveys like Spitzer DeepDrill survey and X-ray surveys like XMM-SERVS, we will be able to select unprecedentedly large samples of quasars, especially

low-luminosity quasars, to study their disk-corona connection.

We thank the anonymous referee for constructive feedback. We thank Chien-Ting Chen, Yuming Fu, Qi Hao, Linhua Jiang, and Xue-Bing Wu for helpful discussions. J.H. and B.L. acknowledge financial support from the National Natural Science Foundation of China grant 11991053 and 11991050, China Manned Space Project grants NO. CMS-CSST-2021-A05 and NO. CMS-CSST-2021-A06, and CNSA program D050102. W.N.B. acknowledges support from NSF grants AST-2106990 and AST-2407089 and the Penn State Eberly Endowment. Y.Q.X. acknowledges financial support from the National Natural Science Foundation of China grants 12025303 and 1239814. The MMT spectra reported here were obtained at the MMT Observatory, a joint facility of the Smithsonian Institution and the University of Arizona. The WIYN spectra presented here were based on the observation at the WIYN Observatory, a joint facility of the NSF’s National Optical-Infrared Astronomy Research Laboratory, Indiana University, the University of Wisconsin-Madison, Pennsylvania State University, and Purdue University. The codes and data supporting the results of this study are publicly available on GitHub¹⁷ and have been archived on Zenodo.¹⁸

Software: ASTROPY (Astropy Collaboration et al. 2013, 2018, 2022), DUSTMAPS (Green 2018), OPTUNA (Akiba et al. 2019), SCIKIT-LEARN (Pedregosa et al. 2011), TOPCAT (Taylor 2005), XGBoost (Chen & Guestrin 2016).

REFERENCES

- Aihara, H., Arimoto, N., Armstrong, R., et al. 2018, PASJ, 70, S4, doi: [10.1093/pasj/psx066](https://doi.org/10.1093/pasj/psx066)
- Aihara, H., AlSayyad, Y., Ando, M., et al. 2022, PASJ, 74, 247, doi: [10.1093/pasj/psab122](https://doi.org/10.1093/pasj/psab122)
- Akiba, T., Sano, S., Yanase, T., Ohta, T., & Koyama, M. 2019, in Proceedings of the 25th ACM SIGKDD International Conference on Knowledge Discovery & Data Mining, 2623–2631
- Arcodia, R., Merloni, A., Nandra, K., & Ponti, G. 2019, A&A, 628, A135, doi: [10.1051/0004-6361/201935874](https://doi.org/10.1051/0004-6361/201935874)
- Arnouts, S., Cristiani, S., Moscardini, L., et al. 1999, MNRAS, 310, 540, doi: [10.1046/j.1365-8711.1999.02978.x](https://doi.org/10.1046/j.1365-8711.1999.02978.x)
- Astropy Collaboration, Robitaille, T. P., Tollerud, E. J., et al. 2013, A&A, 558, A33, doi: [10.1051/0004-6361/201322068](https://doi.org/10.1051/0004-6361/201322068)
- Astropy Collaboration, Price-Whelan, A. M., Sipőcz, B. M., et al. 2018, AJ, 156, 123, doi: [10.3847/1538-3881/aabc4f](https://doi.org/10.3847/1538-3881/aabc4f)
- Astropy Collaboration, Price-Whelan, A. M., Lim, P. L., et al. 2022, ApJ, 935, 167, doi: [10.3847/1538-4357/ac7c74](https://doi.org/10.3847/1538-4357/ac7c74)
- Avni, Y., & Tananbaum, H. 1982, ApJL, 262, L17, doi: [10.1086/183903](https://doi.org/10.1086/183903)
- . 1986, ApJ, 305, 83, doi: [10.1086/164230](https://doi.org/10.1086/164230)
- Barvainis, R., Lehár, J., Birkinshaw, M., Falcke, H., & Blundell, K. M. 2005, ApJ, 618, 108, doi: [10.1086/425859](https://doi.org/10.1086/425859)
- Beck, R., Lin, C. A., Ishida, E. E. O., et al. 2017, MNRAS, 468, 4323, doi: [10.1093/mnras/stx687](https://doi.org/10.1093/mnras/stx687)
- Bertin, E., & Arnouts, S. 1996, A&AS, 117, 393, doi: [10.1051/aas:1996164](https://doi.org/10.1051/aas:1996164)

¹⁷ <https://github.com/choubalv-hj/AstroML>.

¹⁸ <https://doi.org/10.5281/zenodo.14321895>.

- Bisogni, S., Risaliti, G., & Lusso, E. 2017, *Frontiers in Astronomy and Space Sciences*, 4, 68, doi: [10.3389/fspas.2017.00068](https://doi.org/10.3389/fspas.2017.00068)
- Bovy, J., Hennawi, J. F., Hogg, D. W., et al. 2011, *ApJ*, 729, 141, doi: [10.1088/0004-637X/729/2/141](https://doi.org/10.1088/0004-637X/729/2/141)
- Bradshaw, E. J., Almaini, O., Hartley, W. G., et al. 2013, *MNRAS*, 433, 194, doi: [10.1093/mnras/stt715](https://doi.org/10.1093/mnras/stt715)
- Brammer, G. B., van Dokkum, P. G., & Coppi, P. 2008, *ApJ*, 686, 1503, doi: [10.1086/591786](https://doi.org/10.1086/591786)
- Brandt, W. N., & Alexander, D. M. 2015, *A&A Rv*, 23, 1, doi: [10.1007/s00159-014-0081-z](https://doi.org/10.1007/s00159-014-0081-z)
- Brandt, W. N., & Hasinger, G. 2005, *ARA&A*, 43, 827, doi: [10.1146/annurev.astro.43.051804.102213](https://doi.org/10.1146/annurev.astro.43.051804.102213)
- Brandt, W. N., Ni, Q., Yang, G., et al. 2018, arXiv e-prints, arXiv:1811.06542, doi: [10.48550/arXiv.1811.06542](https://doi.org/10.48550/arXiv.1811.06542)
- Brusa, M., Civano, F., Comastri, A., et al. 2010, *ApJ*, 716, 348, doi: [10.1088/0004-637X/716/1/348](https://doi.org/10.1088/0004-637X/716/1/348)
- Calderone, G., Guarneri, F., Porru, M., et al. 2024, *A&A*, 683, A34, doi: [10.1051/0004-6361/202346625](https://doi.org/10.1051/0004-6361/202346625)
- Chaini, S., Bagul, A., Deshpande, A., et al. 2023, *MNRAS*, 518, 3123, doi: [10.1093/mnras/stac3336](https://doi.org/10.1093/mnras/stac3336)
- Chen, C. T. J., Brandt, W. N., Luo, B., et al. 2018, *MNRAS*, 478, 2132, doi: [10.1093/mnras/sty1036](https://doi.org/10.1093/mnras/sty1036)
- Chen, T., & Guestrin, C. 2016, in *KDD '16*, Vol. 11, Proceedings of the 22nd ACM SIGKDD International Conference on Knowledge Discovery and Data Mining (ACM), 785–794, doi: [10.1145/2939672.2939785](https://doi.org/10.1145/2939672.2939785)
- Cheng, H., Liu, B. F., Liu, J., et al. 2020, *MNRAS*, 495, 1158, doi: [10.1093/mnras/staa1250](https://doi.org/10.1093/mnras/staa1250)
- Chiaraluce, E., Vagnetti, F., Tombesi, F., & Paolillo, M. 2018, *A&A*, 619, A95, doi: [10.1051/0004-6361/201833631](https://doi.org/10.1051/0004-6361/201833631)
- Coil, A. L., Blanton, M. R., Burles, S. M., et al. 2011, *ApJ*, 741, 8, doi: [10.1088/0004-637X/741/1/8](https://doi.org/10.1088/0004-637X/741/1/8)
- Diamond-Stanic, A. M., Fan, X., Brandt, W. N., et al. 2009, *ApJ*, 699, 782, doi: [10.1088/0004-637X/699/1/782](https://doi.org/10.1088/0004-637X/699/1/782)
- Falcke, H., Sherwood, W., & Patnaik, A. R. 1996, *ApJ*, 471, 106, doi: [10.1086/177956](https://doi.org/10.1086/177956)
- Fan, L. L., Wang, H. Y., Wang, T., et al. 2009, *ApJ*, 690, 1006, doi: [10.1088/0004-637X/690/1/1006](https://doi.org/10.1088/0004-637X/690/1/1006)
- Fitzpatrick, E. L., Massa, D., Gordon, K. D., Bohlin, R., & Clayton, G. C. 2019, *ApJ*, 886, 108, doi: [10.3847/1538-4357/ab4c3a](https://doi.org/10.3847/1538-4357/ab4c3a)
- Fu, S., Brandt, W. N., Zou, F., et al. 2022, *ApJ*, 934, 97, doi: [10.3847/1538-4357/ac7a36](https://doi.org/10.3847/1538-4357/ac7a36)
- Fu, Y., Wu, X.-B., Yang, Q., et al. 2021, *ApJS*, 254, 6, doi: [10.3847/1538-4365/abe85e](https://doi.org/10.3847/1538-4365/abe85e)
- Fu, Y., Wu, X.-B., Li, Y., et al. 2024, *ApJS*, 271, 54, doi: [10.3847/1538-4365/ad2ae6](https://doi.org/10.3847/1538-4365/ad2ae6)
- Gallagher, S. C., Brandt, W. N., Chartas, G., & Garmire, G. P. 2002, *ApJ*, 567, 37, doi: [10.1086/338485](https://doi.org/10.1086/338485)
- Gallagher, S. C., Brandt, W. N., Chartas, G., et al. 2006, *ApJ*, 644, 709, doi: [10.1086/503762](https://doi.org/10.1086/503762)
- Gao, D., Zhang, Y.-X., & Zhao, Y.-H. 2008, *MNRAS*, 386, 1417, doi: [10.1111/j.1365-2966.2008.13070.x](https://doi.org/10.1111/j.1365-2966.2008.13070.x)
- Garilli, B., Guzzo, L., Scodreggio, M., et al. 2014, *A&A*, 562, A23, doi: [10.1051/0004-6361/201322790](https://doi.org/10.1051/0004-6361/201322790)
- Gehrels, N. 1986, *ApJ*, 303, 336, doi: [10.1086/164079](https://doi.org/10.1086/164079)
- Gibson, R. R., & Brandt, W. N. 2012, *ApJ*, 746, 54, doi: [10.1088/0004-637X/746/1/54](https://doi.org/10.1088/0004-637X/746/1/54)
- Gibson, R. R., Brandt, W. N., Gallagher, S. C., & Schneider, D. P. 2009, *ApJ*, 696, 924, doi: [10.1088/0004-637X/696/1/924](https://doi.org/10.1088/0004-637X/696/1/924)
- Gibson, R. R., Brandt, W. N., & Schneider, D. P. 2008, *ApJ*, 685, 773, doi: [10.1086/590403](https://doi.org/10.1086/590403)
- Golob, A., Sawicki, M., Goulding, A. D., & Coupon, J. 2021, *MNRAS*, 503, 4136, doi: [10.1093/mnras/stab719](https://doi.org/10.1093/mnras/stab719)
- Gordon, K. D., Clayton, G. C., Misselt, K. A., Landolt, A. U., & Wolff, M. J. 2003, *ApJ*, 594, 279, doi: [10.1086/376774](https://doi.org/10.1086/376774)
- Green, G. 2018, *The Journal of Open Source Software*, 3, 695
- Green, P. J., Aldcroft, T. L., Richards, G. T., et al. 2009, *ApJ*, 690, 644, doi: [10.1088/0004-637X/690/1/644](https://doi.org/10.1088/0004-637X/690/1/644)
- Greene, J., Bezanson, R., Ouchi, M., Silverman, J., & the PFS Galaxy Evolution Working Group. 2022, arXiv e-prints, arXiv:2206.14908, doi: [10.48550/arXiv.2206.14908](https://doi.org/10.48550/arXiv.2206.14908)
- Grupe, D., Komossa, S., Leighly, K. M., & Page, K. L. 2010, *ApJS*, 187, 64, doi: [10.1088/0067-0049/187/1/64](https://doi.org/10.1088/0067-0049/187/1/64)
- Hall, P. B., Gallagher, S. C., Richards, G. T., et al. 2006, *AJ*, 132, 1977, doi: [10.1086/507842](https://doi.org/10.1086/507842)
- Heywood, I., Hale, C. L., Jarvis, M. J., et al. 2020, *MNRAS*, 496, 3469, doi: [10.1093/mnras/staa1770](https://doi.org/10.1093/mnras/staa1770)
- Heywood, I., Jarvis, M. J., Hale, C. L., et al. 2022, *MNRAS*, 509, 2150, doi: [10.1093/mnras/stab3021](https://doi.org/10.1093/mnras/stab3021)
- HI4PI Collaboration, Ben Bekhti, N., Flöer, L., et al. 2016, *A&A*, 594, A116, doi: [10.1051/0004-6361/201629178](https://doi.org/10.1051/0004-6361/201629178)
- Hildebrandt, H., Arnouts, S., Capak, P., et al. 2010, *A&A*, 523, A31, doi: [10.1051/0004-6361/201014885](https://doi.org/10.1051/0004-6361/201014885)
- Huang, J., Luo, B., Brandt, W. N., et al. 2023, *ApJ*, 950, 18, doi: [10.3847/1538-4357/accd64](https://doi.org/10.3847/1538-4357/accd64)
- Hudelot, P., Cuillandre, J. C., Withington, K., et al. 2012, *VizieR Online Data Catalog*, II/317
- Hughes, A. C. N., Bailer-Jones, C. A. L., & Jamal, S. 2022, *A&A*, 668, A99, doi: [10.1051/0004-6361/202244859](https://doi.org/10.1051/0004-6361/202244859)
- Ilbert, O., Arnouts, S., McCracken, H. J., et al. 2006, *A&A*, 457, 841, doi: [10.1051/0004-6361:20065138](https://doi.org/10.1051/0004-6361:20065138)
- Isobe, T., & Feigelson, E. D. 1990, in *Bulletin of the American Astronomical Society*, Vol. 22, 917–918

- Jarvis, M. J., Bonfield, D. G., Bruce, V. A., et al. 2013, *MNRAS*, 428, 1281, doi: [10.1093/mnras/sts118](https://doi.org/10.1093/mnras/sts118)
- Jiang, L., Fan, X., Ivezić, Ž., et al. 2007, *ApJ*, 656, 680, doi: [10.1086/510831](https://doi.org/10.1086/510831)
- Jin, C., Lusso, E., Ward, M., Done, C., & Middei, R. 2024, *MNRAS*, 527, 356, doi: [10.1093/mnras/stad3193](https://doi.org/10.1093/mnras/stad3193)
- Jin, C., Ward, M., & Done, C. 2012, *MNRAS*, 422, 3268, doi: [10.1111/j.1365-2966.2012.20847.x](https://doi.org/10.1111/j.1365-2966.2012.20847.x)
- Jin, X., Zhang, Y., Zhang, J., et al. 2019, *MNRAS*, 485, 4539, doi: [10.1093/mnras/stz680](https://doi.org/10.1093/mnras/stz680)
- Just, D. W., Brandt, W. N., Shemmer, O., et al. 2007, *ApJ*, 665, 1004, doi: [10.1086/519990](https://doi.org/10.1086/519990)
- Kellermann, K. I., Sramek, R., Schmidt, M., Shaffer, D. B., & Green, R. 1989, *AJ*, 98, 1195, doi: [10.1086/115207](https://doi.org/10.1086/115207)
- Krawczyk, C. M., Richards, G. T., Mehta, S. S., et al. 2013, *ApJS*, 206, 4, doi: [10.1088/0067-0049/206/1/4](https://doi.org/10.1088/0067-0049/206/1/4)
- Kriss, G. A., & Canizares, C. R. 1985, *ApJ*, 297, 177, doi: [10.1086/163514](https://doi.org/10.1086/163514)
- Kubota, A., & Done, C. 2018, *MNRAS*, 480, 1247, doi: [10.1093/mnras/sty1890](https://doi.org/10.1093/mnras/sty1890)
- Lacy, M., Surace, J. A., Farrah, D., et al. 2020, DeepDrill XMM-LSS 2-band Catalog, the Infrared Science Archive (IRSA), doi: [10.26131/IRSA500](https://doi.org/10.26131/IRSA500)
- . 2021, *MNRAS*, 501, 892, doi: [10.1093/mnras/staa3714](https://doi.org/10.1093/mnras/staa3714)
- Laha, S., Ghosh, R., Guainazzi, M., & Markowitz, A. G. 2018, *MNRAS*, 480, 1522, doi: [10.1093/mnras/sty1919](https://doi.org/10.1093/mnras/sty1919)
- Laor, A., & Davis, S. W. 2011, *MNRAS*, 417, 681, doi: [10.1111/j.1365-2966.2011.19310.x](https://doi.org/10.1111/j.1365-2966.2011.19310.x)
- Lavalley, M., Isobe, T., & Feigelson, E. 1992, in *Astronomical Society of the Pacific Conference Series*, Vol. 25, *Astronomical Data Analysis Software and Systems I*, ed. D. M. Worrall, C. Biemesderfer, & J. Barnes, 245
- Le Fèvre, O., Cassata, P., Cucciati, O., et al. 2013, *A&A*, 559, A14, doi: [10.1051/0004-6361/201322179](https://doi.org/10.1051/0004-6361/201322179)
- Li, C., Zhang, Y., Cui, C., et al. 2022, *MNRAS*, 509, 2289, doi: [10.1093/mnras/stab3165](https://doi.org/10.1093/mnras/stab3165)
- Liu, H., Luo, B., Brandt, W. N., et al. 2021, *ApJ*, 910, 103, doi: [10.3847/1538-4357/abe37f](https://doi.org/10.3847/1538-4357/abe37f)
- . 2022, *ApJ*, 930, 53, doi: [10.3847/1538-4357/ac6265](https://doi.org/10.3847/1538-4357/ac6265)
- . 2019, *ApJ*, 878, 79, doi: [10.3847/1538-4357/ab1d5b](https://doi.org/10.3847/1538-4357/ab1d5b)
- Luo, B., Brandt, W. N., Xue, Y. Q., et al. 2010, *ApJS*, 187, 560, doi: [10.1088/0067-0049/187/2/560](https://doi.org/10.1088/0067-0049/187/2/560)
- Luo, B., Brandt, W. N., Hall, P. B., et al. 2015, *ApJ*, 805, 122, doi: [10.1088/0004-637X/805/2/122](https://doi.org/10.1088/0004-637X/805/2/122)
- Lusso, E., & Risaliti, G. 2016, *ApJ*, 819, 154, doi: [10.3847/0004-637X/819/2/154](https://doi.org/10.3847/0004-637X/819/2/154)
- . 2017, *A&A*, 602, A79, doi: [10.1051/0004-6361/201630079](https://doi.org/10.1051/0004-6361/201630079)
- Lusso, E., Comastri, A., Vignali, C., et al. 2010, *A&A*, 512, A34, doi: [10.1051/0004-6361/200913298](https://doi.org/10.1051/0004-6361/200913298)
- Lusso, E., Risaliti, G., Nardini, E., et al. 2020, *A&A*, 642, A150, doi: [10.1051/0004-6361/202038899](https://doi.org/10.1051/0004-6361/202038899)
- Lyke, B. W., Higley, A. N., McLane, J. N., et al. 2020, *ApJS*, 250, 8, doi: [10.3847/1538-4365/aba623](https://doi.org/10.3847/1538-4365/aba623)
- MacLeod, C. L., Ivezić, Ž., Kochanek, C. S., et al. 2010, *ApJ*, 721, 1014, doi: [10.1088/0004-637X/721/2/1014](https://doi.org/10.1088/0004-637X/721/2/1014)
- Maiolino, R., Cirasuolo, M., Afonso, J., et al. 2020, *The Messenger*, 180, 24, doi: [10.18727/0722-6691/5197](https://doi.org/10.18727/0722-6691/5197)
- Marchesi, S., Civano, F., Elvis, M., et al. 2016, *ApJ*, 817, 34, doi: [10.3847/0004-637X/817/1/34](https://doi.org/10.3847/0004-637X/817/1/34)
- Martin, D. C., Fanson, J., Schiminovich, D., et al. 2005, *ApJL*, 619, L1, doi: [10.1086/426387](https://doi.org/10.1086/426387)
- Martínez-Solaesche, G., Queiroz, C., González Delgado, R. M., et al. 2023, *A&A*, 673, A103, doi: [10.1051/0004-6361/202245750](https://doi.org/10.1051/0004-6361/202245750)
- McHardy, I. M., Koerding, E., Knigge, C., Uttley, P., & Fender, R. P. 2006, *Nature*, 444, 730, doi: [10.1038/nature05389](https://doi.org/10.1038/nature05389)
- McLure, R. J., Pearce, H. J., Dunlop, J. S., et al. 2013, *MNRAS*, 428, 1088, doi: [10.1093/mnras/sts092](https://doi.org/10.1093/mnras/sts092)
- Miller, B. P., Brandt, W. N., Schneider, D. P., et al. 2011, *ApJ*, 726, 20, doi: [10.1088/0004-637X/726/1/20](https://doi.org/10.1088/0004-637X/726/1/20)
- Miniutti, G., Brandt, W. N., Schneider, D. P., et al. 2012, *MNRAS*, 425, 1718, doi: [10.1111/j.1365-2966.2012.21648.x](https://doi.org/10.1111/j.1365-2966.2012.21648.x)
- Mirabal, N., Charles, E., Ferrara, E. C., et al. 2016, *ApJ*, 825, 69, doi: [10.3847/0004-637X/825/1/69](https://doi.org/10.3847/0004-637X/825/1/69)
- Miyazaki, S., Komiyama, Y., Kawanomoto, S., et al. 2018, *PASJ*, 70, S1, doi: [10.1093/pasj/psx063](https://doi.org/10.1093/pasj/psx063)
- Momcheva, I. G., Brammer, G. B., van Dokkum, P. G., et al. 2016, *ApJS*, 225, 27, doi: [10.3847/0067-0049/225/2/27](https://doi.org/10.3847/0067-0049/225/2/27)
- Ni, Q., Brandt, W. N., Luo, B., et al. 2018, *MNRAS*, 480, 5184, doi: [10.1093/mnras/sty1989](https://doi.org/10.1093/mnras/sty1989)
- Ni, Q., Brandt, W. N., Yi, W., et al. 2020, *ApJL*, 889, L37, doi: [10.3847/2041-8213/ab6d78](https://doi.org/10.3847/2041-8213/ab6d78)
- Ni, Q., Brandt, W. N., Chen, C.-T., et al. 2021, *ApJS*, 256, 21, doi: [10.3847/1538-4365/ac0dc6](https://doi.org/10.3847/1538-4365/ac0dc6)
- Ni, Q., Brandt, W. N., Luo, B., et al. 2022, *MNRAS*, 511, 5251, doi: [10.1093/mnras/stac394](https://doi.org/10.1093/mnras/stac394)
- Pedregosa, F., Varoquaux, G., Gramfort, A., et al. 2011, *Journal of Machine Learning Research*, 12, 2825
- Peng, N., Zhang, Y., Zhao, Y., & Wu, X.-b. 2012, *MNRAS*, 425, 2599, doi: [10.1111/j.1365-2966.2012.21191.x](https://doi.org/10.1111/j.1365-2966.2012.21191.x)
- Planck Collaboration, Aghanim, N., Akrami, Y., et al. 2020, *A&A*, 641, A6, doi: [10.1051/0004-6361/201833910](https://doi.org/10.1051/0004-6361/201833910)
- Plotkin, R. M., Anderson, S. F., Brandt, W. N., et al. 2010, *ApJ*, 721, 562, doi: [10.1088/0004-637X/721/1/562](https://doi.org/10.1088/0004-637X/721/1/562)

- Pu, X., Luo, B., Brandt, W. N., et al. 2020, *ApJ*, 900, 141, doi: [10.3847/1538-4357/abacc5](https://doi.org/10.3847/1538-4357/abacc5)
- Rankine, A. L., Aird, J., Ruiz, A., & Georgakakis, A. 2024, *MNRAS*, 527, 9004, doi: [10.1093/mnras/stad3686](https://doi.org/10.1093/mnras/stad3686)
- Richards, G. T., Nichol, R. C., Gray, A. G., et al. 2004, *ApJS*, 155, 257, doi: [10.1086/425356](https://doi.org/10.1086/425356)
- Richards, G. T., Strauss, M. A., Fan, X., et al. 2006, *AJ*, 131, 2766, doi: [10.1086/503559](https://doi.org/10.1086/503559)
- Rosen, S. R., Webb, N. A., Watson, M. G., et al. 2016, *A&A*, 590, A1, doi: [10.1051/0004-6361/201526416](https://doi.org/10.1051/0004-6361/201526416)
- Salvato, M., Ilbert, O., & Hoyle, B. 2019, *Nature Astronomy*, 3, 212, doi: [10.1038/s41550-018-0478-0](https://doi.org/10.1038/s41550-018-0478-0)
- Salvato, M., Hasinger, G., Ilbert, O., et al. 2009, *ApJ*, 690, 1250, doi: [10.1088/0004-637X/690/2/1250](https://doi.org/10.1088/0004-637X/690/2/1250)
- Sánchez, C., Carrasco Kind, M., Lin, H., et al. 2014, *MNRAS*, 445, 1482, doi: [10.1093/mnras/stu1836](https://doi.org/10.1093/mnras/stu1836)
- Sawicki, M., Arnouts, S., Huang, J., et al. 2019, *MNRAS*, 489, 5202, doi: [10.1093/mnras/stz2522](https://doi.org/10.1093/mnras/stz2522)
- Schlegel, D. J., Finkbeiner, D. P., & Davis, M. 1998, *ApJ*, 500, 525, doi: [10.1086/305772](https://doi.org/10.1086/305772)
- Schmidt, M., & Green, R. F. 1983, *ApJ*, 269, 352, doi: [10.1086/161048](https://doi.org/10.1086/161048)
- Schmidt, S. J., Malz, A. I., Soo, J. Y. H., et al. 2020, *MNRAS*, 499, 1587, doi: [10.1093/mnras/staa2799](https://doi.org/10.1093/mnras/staa2799)
- Scolnic, D. M., Lochner, M., Gris, P., et al. 2018, *arXiv e-prints*, arXiv:1812.00516, doi: [10.48550/arXiv.1812.00516](https://doi.org/10.48550/arXiv.1812.00516)
- Shemmer, O., Brandt, W. N., Anderson, S. F., et al. 2009, *ApJ*, 696, 580, doi: [10.1088/0004-637X/696/1/580](https://doi.org/10.1088/0004-637X/696/1/580)
- Shemmer, O., Brandt, W. N., Netzer, H., Maiolino, R., & Kaspi, S. 2008, *ApJ*, 682, 81, doi: [10.1086/588776](https://doi.org/10.1086/588776)
- Shen, Y., Richards, G. T., Strauss, M. A., et al. 2011, *ApJS*, 194, 45, doi: [10.1088/0067-0049/194/2/45](https://doi.org/10.1088/0067-0049/194/2/45)
- Signorini, M., Risaliti, G., Lusso, E., et al. 2023, *A&A*, 676, A143, doi: [10.1051/0004-6361/202346104](https://doi.org/10.1051/0004-6361/202346104)
- Skelton, R. E., Whitaker, K. E., Momcheva, I. G., et al. 2014, *ApJS*, 214, 24, doi: [10.1088/0067-0049/214/2/24](https://doi.org/10.1088/0067-0049/214/2/24)
- Steffen, A. T., Strateva, I., Brandt, W. N., et al. 2006, *AJ*, 131, 2826, doi: [10.1086/503627](https://doi.org/10.1086/503627)
- Strateva, I. V., Brandt, W. N., Schneider, D. P., Vanden Berk, D. G., & Vignali, C. 2005, *AJ*, 130, 387, doi: [10.1086/431247](https://doi.org/10.1086/431247)
- Strüder, L., Briel, U., Dennerl, K., et al. 2001, *A&A*, 365, L18, doi: [10.1051/0004-6361:20000066](https://doi.org/10.1051/0004-6361:20000066)
- Swann, E., Sullivan, M., Carrick, J., et al. 2019, *The Messenger*, 175, 58, doi: [10.18727/0722-6691/5129](https://doi.org/10.18727/0722-6691/5129)
- Tanaka, M., Coupon, J., Hsieh, B.-C., et al. 2018, *PASJ*, 70, S9, doi: [10.1093/pasj/psx077](https://doi.org/10.1093/pasj/psx077)
- Tananbaum, H., Avni, Y., Branduardi, G., et al. 1979, *ApJL*, 234, L9, doi: [10.1086/183100](https://doi.org/10.1086/183100)
- Taylor, M. B. 2005, in *Astronomical Society of the Pacific Conference Series*, Vol. 347, *Astronomical Data Analysis Software and Systems XIV*, ed. P. Shopbell, M. Britton, & R. Ebert, 29
- Timlin, John D., I., Brandt, W. N., Zhu, S., et al. 2020a, *MNRAS*, 498, 4033, doi: [10.1093/mnras/staa2661](https://doi.org/10.1093/mnras/staa2661)
- Timlin, J. D., Brandt, W. N., Ni, Q., et al. 2020b, *MNRAS*, 492, 719, doi: [10.1093/mnras/stz3433](https://doi.org/10.1093/mnras/stz3433)
- Traulsen, I., Schwobe, A. D., Lamer, G., et al. 2020, *A&A*, 641, A137, doi: [10.1051/0004-6361/202037706](https://doi.org/10.1051/0004-6361/202037706)
- Tuccillo, D., González-Serrano, J. I., & Benn, C. R. 2015, *MNRAS*, 449, 2818, doi: [10.1093/mnras/stv472](https://doi.org/10.1093/mnras/stv472)
- Vagnetti, F., Antonucci, M., & Trevese, D. 2013, *A&A*, 550, A71, doi: [10.1051/0004-6361/201220443](https://doi.org/10.1051/0004-6361/201220443)
- Vagnetti, F., Turriziani, S., Trevese, D., & Antonucci, M. 2010, *A&A*, 519, A17, doi: [10.1051/0004-6361/201014320](https://doi.org/10.1051/0004-6361/201014320)
- Vanden Berk, D. E., Richards, G. T., Bauer, A., et al. 2001, *AJ*, 122, 549, doi: [10.1086/321167](https://doi.org/10.1086/321167)
- Vignali, C., Brandt, W. N., & Schneider, D. P. 2003, *AJ*, 125, 433, doi: [10.1086/345973](https://doi.org/10.1086/345973)
- Vignali, C., Brandt, W. N., Schneider, D. P., & Kaspi, S. 2005, *AJ*, 129, 2519, doi: [10.1086/430217](https://doi.org/10.1086/430217)
- Walter, R., & Fink, H. H. 1993, *A&A*, 274, 105
- Wang, C., Luo, B., Brandt, W. N., et al. 2022, *ApJ*, 936, 95, doi: [10.3847/1538-4357/ac886e](https://doi.org/10.3847/1538-4357/ac886e)
- Wang, S., Brandt, W. N., Luo, B., et al. 2024, *ApJ*, 974, 2, doi: [10.3847/1538-4357/ad7589](https://doi.org/10.3847/1538-4357/ad7589)
- Webb, N. A., Coriat, M., Traulsen, I., et al. 2020, *A&A*, 641, A136, doi: [10.1051/0004-6361/201937353](https://doi.org/10.1051/0004-6361/201937353)
- Wilkes, B. J., Tananbaum, H., Worrall, D. M., et al. 1994, *ApJS*, 92, 53, doi: [10.1086/191959](https://doi.org/10.1086/191959)
- Wolf, C., Meisenheimer, K., Kleinheinrich, M., et al. 2004, *A&A*, 421, 913, doi: [10.1051/0004-6361:20040525](https://doi.org/10.1051/0004-6361:20040525)
- Wu, J., Brandt, W. N., Anderson, S. F., et al. 2012, *ApJ*, 747, 10, doi: [10.1088/0004-637X/747/1/10](https://doi.org/10.1088/0004-637X/747/1/10)
- Xue, Y. Q. 2017, *NewAR*, 79, 59, doi: [10.1016/j.newar.2017.09.002](https://doi.org/10.1016/j.newar.2017.09.002)
- Yang, G., Brandt, W. N., Luo, B., et al. 2016, *ApJ*, 831, 145, doi: [10.3847/0004-637X/831/2/145](https://doi.org/10.3847/0004-637X/831/2/145)
- Yang, Q., & Shen, Y. 2023, *ApJS*, 264, 9, doi: [10.3847/1538-4365/ac9ea8](https://doi.org/10.3847/1538-4365/ac9ea8)
- Yang, Q., Wu, X.-B., Fan, X., et al. 2017, *AJ*, 154, 269, doi: [10.3847/1538-3881/aa943c](https://doi.org/10.3847/1538-3881/aa943c)
- Yèche, C., Petitjean, P., Rich, J., et al. 2010, *A&A*, 523, A14, doi: [10.1051/0004-6361/200913508](https://doi.org/10.1051/0004-6361/200913508)
- Young, M., Elvis, M., & Risaliti, G. 2010, *ApJ*, 708, 1388, doi: [10.1088/0004-637X/708/2/1388](https://doi.org/10.1088/0004-637X/708/2/1388)
- Zhan, H. 2011, *Scientia Sinica Physica, Mechanica & Astronomica*, 41, 1441, doi: [10.1360/132011-961](https://doi.org/10.1360/132011-961)

Zhang, Z., Luo, B., Brandt, W. N., et al. 2023, ApJ, 954, 159, doi: [10.3847/1538-4357/ace7c2](https://doi.org/10.3847/1538-4357/ace7c2)
Zheng, X. C., Xue, Y. Q., Brandt, W. N., et al. 2017, ApJ, 849, 127, doi: [10.3847/1538-4357/aa9378](https://doi.org/10.3847/1538-4357/aa9378)
Zhu, S., Brandt, W. N., Zou, F., et al. 2023, MNRAS, 522, 3506, doi: [10.1093/mnras/stad1178](https://doi.org/10.1093/mnras/stad1178)

Zhu, S. F., Brandt, W. N., Luo, B., et al. 2020, MNRAS, 496, 245, doi: [10.1093/mnras/staa1411](https://doi.org/10.1093/mnras/staa1411)
Zou, F., Brandt, W. N., Chen, C.-T., et al. 2022, ApJS, 262, 15, doi: [10.3847/1538-4365/ac7bdf](https://doi.org/10.3847/1538-4365/ac7bdf)